Journal of Wind Engineering & Industrial Aerodynamics 245 (2024) 105615

Contents lists available at ScienceDirect

Journal of Wind Engineering & Industrial Aerodynamics

journal homepage: www.elsevier.com/locate/jweia

Parametric effects of turbulence on the flutter stability of suspension bridges

Niccolò Barni *, Claudio Mannini

CRIACIV/Department of Civil and Environmental Engineering, University of Florence, Via S. Marta 3, 50139, Florence, Italy

ARTICLE INFO

Keywords:
Suspension bridges
Flutter stability
Turbulent flow
Nonlinear self-excited forces
Time-variant system
Monte-Carlo simulations
Floquet theory

ABSTRACT

Despite extensive past research efforts, the influence of turbulence on suspension bridge flutter stability has not been fully understood yet. Moreover, the role of large-scale turbulence has been overlooked in predicting the critical wind velocity, despite experimental and numerical studies indicating that atmospheric turbulence can have either a stabilising or a destabilising effect. This study investigates the parametric effects of large-scale turbulence on flutter stability based on the 2D Rational Function Approximation model, considering the Hardanger Bridge, in Norway, as a case study. First, a Monte Carlo method is used to analyse the bridge stability under various turbulent wind conditions, considering turbulence intensity and integral length scale as key parameters. The results highlight the sensitivity of flutter stability to these turbulence parameters, as well as essentially its independence of the spanwise correlation of the parametric excitation. The role of the variation in the wind angle of attack is found to be largely dominant compared to that in the wind velocity magnitude. Subsequently, Floquet multipliers are employed to study the influence of periodic parametric excitations on bridge stability, assuming sinusoidal fluctuations of wind velocity magnitude and angle of attack. This simplified scenario helps us understand the various parametric excitation mechanisms and explain the results of the more realistic Monte Carlo approach. The study emphasises the key role played in flutter stability and buffeting response by the so-called "average parametric effect", associated with the mean of the aerodynamic derivatives as nonlinear functions of the slowly-varying angle of attack. The preponderance of this effect in most realistic turbulent wind scenarios also explains the negligible impact of correlation of the parametric variation in the angle of attack. Finally, an equivalent linear time-invariant model is proposed to account for the parametric effects of turbulence in a simple way, yielding good results and offering a new perspective on the use of classical self-excited force coefficients.

1. Introduction

At the dawn of a new era of super-long suspension bridges launched by the latest opening of the Çanakkale Bridge, Turkey, there is the perception that new challenges for wind engineers may appear for such unexplored structural flexibility. As a matter of fact, despite several decades of research on wind-induced aeroelastic phenomena for long-span suspension bridges, the increasing scale of these structures, such as the Messina and Gibraltar crossings with spans reaching 3000 m, presents new and potentially more complex issues. Although suspension bridge designs have not encountered critical problems thus far, as the demand for long-span crossings continues to grow, the accuracy of bridge response and stability assessment has been becoming increasingly crucial. Indeed, the dynamic response to wind excitation can significantly impact the design stresses experienced by the bridge (Davenport, 1962; Aas-Jakobsen and Strømmen, 2001; Lystad et al., 2020; Barni et al., 2023a). Consequently, enhancing our understanding of wind-induced aeroelastic phenomena and refining mathematical models is imperative for the feasibility and to ensure the safety of these extraordinary structures.

Assuming a linear behaviour for both the structure and the aerodynamic loads, the problem of bridge flutter stability has extensively been addressed in both the frequency and the time domain. In most studies (e.g., Scanlan, 1978; Jain et al., 1996; Katsuchi et al., 1999; Chen and Kareem, 2006; Bartoli and Mannini, 2008), deterministic flutter stability thresholds have been estimated neglecting both the uncertainty in self-excited force coefficients and the effect of atmospheric turbulence. Nevertheless, free-stream turbulence, defects in the experimental setup, identification techniques, and limitations in the underlying mathematical models can introduce uncertainty in the aerodynamic derivatives (Caracoglia et al., 2009; Caracoglia, 2013; Mannini and Bartoli, 2015; Scanlan and Lin, 1978; Rizzo and Caracoglia, 2018; Sarkar

* Corresponding author.
E-mail addresses: niccolo.barni@unifi.it (N. Barni), claudio.mannini@unifi.it (C. Mannini).

https://doi.org/10.1016/j.jweia.2023.105615
Received 28 July 2023; Received in revised form 30 October 2023; Accepted 23 November 2023

et al., 2009). In recent years, a few probabilistic approaches have been employed in flutter stability analysis, considering Gaussian random sources of uncertainty in the aerodynamic derivatives (Seo and Caracoglia, 2011; Argentini et al., 2014; Canor et al., 2015; Mannini and Bartoli, 2015), aiming at determining the flutter failure probability for a given mean wind velocity.

As for atmospheric turbulence, it is now well established that it can alter the aerodynamic derivatives, both through small scales (e.g., Bearman and Morel, 1983; Mannini et al., 2018), which interact with shear layer separation, and through large scales, which locally change kinetic pressure and incident wind slope. Then, large-scale atmospheric turbulence can introduce various sources of randomness in the parameters of self-excited forces. In particular, in the early 1980s, Lin and Ariaratnam (1980) addressed the random fluctuations in the kinetic pressure by studying the almost sure stability of a bridge and determining statistical moment boundaries. This pioneering work was the first attempt to consider the influence of longitudinal turbulence on bridge stability, specifically focusing on torsional motion. They assumed a white-noise random variation in the wind velocity magnitude, which parametrically affects aerodynamic damping and stiffness. Such a simplified model for turbulence leads to a bridge response that can approximately be considered a Markov vector, thus facilitating the study of the stochastic differential equation stability. The approximation of the turbulence spectrum with a white noise is supported by assuming a Mathieu-Hill behaviour for the dynamic system, exhibiting both parametric damping and stiffness. Indeed, the strongest parametric excitation is exhibited at two times the vibration frequency, as described by Kozin (1967). Therefore, the spectral density level at this frequency becomes the most crucial modelling parameter for longitudinal turbulence. Unlike some previous experiments (Irwin and Schuyler, 1978), Lin and Ariaratnam (1980) concluded that turbulence can potentially cause instability in an otherwise stable system. Building upon this, Bucher and Lin (1988a) studied the stability of the second statistical moment of a two-degree of freedom system with different bridge cross-sections. They found that random variations in the wind velocity can stabilise coupled flutter, as the random parametric excitation leads to an energy transfer from the critical modes to more stable modes. Moreover, the partial correlation of velocity fluctuations makes possible such a transfer between modes of the same type (e.g., different torsional modes), reducing at the same time the parametric excitation of lower order modes (Bucher and Lin, 1988b). Then, using the stochastic average approach, Bucher and Lin (1989) made progress in efficiently assessing moment stability. In the same period, Tsiatas and Sarkar (1988) conducted a similar study focusing on the root mean square (RMS) of the bridge response up to the flutter instability onset. They utilised stochastic calculus to examine the effects of wide-band weakly-stationary random perturbations in the longitudinal and vertical wind velocity components, including also the analysis of the effect of spatial correlation in the buffeting forces. They found that turbulence could destabilise the system, leading to a reduction in the flutter stability threshold. Later, Lin and Li (1993) improved the understanding of the phenomenon by removing the simplified white-noise assumption and introducing a new turbulence model capable of representing various broad-band processes by simply adjusting a few parameters. Depending on the type of turbulence spectrum and turbulence intensity considered, they observed both stabilising and destabilising effects. In the early 2000s, Poirel and Price (2001, 2003) included the effects of the vertical component of wind velocity fluctuations for a 2-DoF airfoil, obtaining the stochastic stability boundaries by numerical estimation of the largest Lyapunov exponent. The sensitivity of stochastic stability to turbulence parameters, such as intensity and integral length scale, as well as to structural parameters, was also studied. The results were consistent with those obtained by Lin and Ariaratnam (1980) and Tsiatas and Sarkar (1988), confirming the destabilising role of turbulence. In particular, a more unstable condition was obtained by increasing the turbulence length scale, highlighting the crucial role of large-scale (low-frequency) turbulent fluctuations. In Poirel and Price (2001, 2003) and in Lin and Lin (1995), parametric resonances due to a narrow-band excitation were also thoroughly investigated using the averaging method of Bogoliubov and Mitroplosky (1961). This extreme simplification of turbulence effects allowed underlining the primary resonance at twice the flutter frequency, typically observed in time-variant dynamical systems. All the approaches described above consider the turbulent perturbation only in the kinetic pressure that scales the self-excited forces, but the indicial function or the rational approximation characterising the self-excited forces are considered unchanged (see assumption b in Lin and Ariaratnam, 1980), thus neglecting the variation in the reduced wind velocity produced by the turbulent fluctuations. This might be a shortcoming when the aerodynamic derivatives show large gradients with the reduced velocity, thus significantly varying aerodynamic damping and stiffness and leading to parametric excitation phenomena. Furthermore, all these studies are based on the assumption of small oscillations of both the bridge and the fluid around the steady-state configuration.

In addition to the parametric effect associated with the kinetic pressure, large-scale turbulence also changes in time the angle of attack, which is known to affect the aerodynamic derivatives (e.g., Argentini et al., 2020; Barni et al., 2021) and, therefore, implies a random variation in the bridge aerodynamics. The attention to this effect originated from Prof. Diana and co-workers' studies, who first recognised the significance of this effect for bridge buffeting response (Bocciolone et al., 1992). Then, its modelling has extensively been pursued over the past three decades, leading to the development of various nonlinear force models that account for the low-frequency modulation of self-excited forces caused by large-scale turbulence (Diana et al., 1993, 1995, 2013; Chen and Kareem, 2001; Diana and Omarini, 2020; Barni et al., 2021). Along this line of research, Barni et al. (2022) incorporated the model proposed in Barni et al. (2021) in a time-variant state-space framework, considering the loss of spanwise correlation of turbulent fluctuations along the girder. The results revealed that turbulence is able to anticipate the flutter stability threshold of the Hardanger Bridge, in Norway (1310 m main span), and this effect was mainly attributed to the torsional aerodynamic damping variation due to the modulation of the aerodynamic coefficient A_2^*. Linear and nonlinear buffeting response and flutter stability of long-span bridges is also the object of an international benchmark organised by the International Association for Bridge and Structural Engineering (https://iabse.org/Committees/Technical-Groups/Task -Groups/Task-Group-31) (Diana et al., 2019, 2020).

All the abovementioned models are usually addressed as "nonlinear" although they rely on a dynamic linearisation of the aerodynamic forces around a slowly-varying angle of attack due to large-scale turbulence. This linearisation does not allow accounting for amplitude-dependent phenomena typical of post-critical flutter states (e.g., limit-cycle oscillations). Nevertheless, it yields a time-variant problem that may exhibit characteristic features of nonlinear system, in the same way as Mathieu or Hill's equations (see, e.g., Nayfeh and Mook, 2008). Moreover, some models also include in the slowly-varying angle of attack the contribution of the background motion of the bridge, which is another source of nonlinearity.

The role played in bridge flutter stability by the spanwise correlation of the parametric excitation is another open issue. Scanlan (1997) suggested that turbulence stabilises the bridge by enhancing the loss of self-excited force correlation along the girder. Similarly, Chen and Kareem (2003) ascribed the limited impact of turbulence on bridge flutter stability to the rapid loss of correlation of wind velocity fluctuations and, consequently, of the parametric excitation caused by turbulence. However, these explanations have not been either experimentally or theoretically demonstrated yet. A reason for this is also the lack of computational efficiency of the models that consider the modulation of self-excited forces along the bridge girder. In this regard, the nonlinear buffeting framework proposed in Barni et al. (2022) has eventually provided an efficient method to account for the

three-dimensional parametric effect of large-scale turbulence.

The current work aims to study the parametric effects of large-scale atmospheric turbulence on bridge flutter stability in terms of variations in both wind velocity magnitude and angle of attack, which have always separately been addressed so far. A multi-degree-of-freedom model of the Hardanger Bridge is considered as a case study. The self-excited force modulation due to large-scale turbulence is considered according to the 2D Rational Function Approximation model (2D RFA), proposed and experimentally validated in Barni et al. (2021), and the time-variant state-space framework reported in Barni et al. (2022). First, the bridge stability is assessed using a Monte Carlo approach, with particular emphasis on the influence of turbulence intensity and integral length scale. This method allows considering the actual large-scale turbulence parametric excitation (no white-noise or similar approximations are needed), leading to a realistic modelling of the phenomena. The impact of the partial correlation of parametric excitations is also easily studied. However, not only does this approach not permit the determination of a formal stability limit (e.g., sample or p-th moment stability thresholds), but it also does not allow any physical understanding of the phenomenon. Consequently, the parametric effects due to turbulence are then investigated by simplifying the parametric excitation assuming a time-periodic wind gust. In this case, the stability boundaries can formally be determined using the theory of Floquet multipliers for time-periodic system. Though strongly simplifying the complex stochastic nature of the problem, this time-periodic approach facilitates the isolation of various parametric effects and allows drawing conclusions regarding their actual impact on the flutter stability and buffeting response of realistic suspension bridges. Finally, an equivalent linear time-invariant model for self-excited forces is proposed by correcting Scanlan's model to account for the major parametric effect of large-scale turbulence.

The paper is structured as follows. Section 2 summarises the implementation of the 2D RFA model for nonlinear bridge buffeting response and flutter stability. The approaches used to determine the parametric effects of turbulence on the bridge dynamic response, namely Monte Carlo simulations and Floquet analysis, are briefly presented in Section 3. The bridge case study and the random wind field characteristics assumed in the calculations are presented in Section 4. Section 5 discusses the main results of the analyses, highlighting how large-scale turbulence parametrically affects the bridge behaviour. Section 6 introduces the linear equivalent model that accounts for most of these parametric effects. Some conclusions are finally drawn in Section 7.

2. Background: time-variant state-space model

Preserving the classical small-vibration hypothesis, the parametric variation of self-excited forces due to large-scale turbulence is addressed in the present work. In particular, assuming that wind velocity magnitude and angle of attack oscillate slowly compared to the bridge motion (in a similar way to Barni et al., 2021, 2022, though in those cases only the variation in the angle of attack was considered), the time-variant transfer function $\mathbf{G}(\widetilde{K},\widetilde{\alpha})$ between the motion vector $\mathbf{r}$ and the self-excited force vector $\mathbf{q}_{se}$ for a three-degree-of-freedom two-dimensional bridge deck model (Fig. 1) maintains the simple form valid for a linear system, but it becomes a function of slowly-varying reduced frequency $\widetilde{K}$ (or reduced wind velocity $2\pi/\widetilde{K}$) and turbulence-induced angle of attack $\widetilde{\alpha}$, where the operator tilde indicates a low-pass filter applied to a certain quantity $(\cdot)$, so that $(\cdot)-\widetilde{(\cdot)}$ denotes the attendant high-frequency component. Theoretically speaking, this is equivalent to linearising the aerodynamic forces around a stochastically varying condition, specifically the slowly-varying wind velocity magnitude and angle of attack. This stands in contrast to the conventional linearisation around a fixed point represented by the mean wind incidence and the static deformed position of the bridge under dead (or dead and static wind) loads. Then, the self-excited forces can be written in the mixed time-frequency domain as follows:

$$\begin{aligned}&\mathbf{q}_{se}\left(\widetilde{K},\widetilde{\alpha},\omega\right)=\mathbf{G}\left(\widetilde{K},\widetilde{\alpha}\right)\mathbf{R}(\omega)\\&\mathbf{q}_{se}=\begin{bmatrix}q_y & q_z & q_\theta\end{bmatrix}^T\\&\mathbf{R}=\mathscr{F}[\mathbf{r}]=\mathscr{F}[y \quad z \quad \theta]^T\end{aligned}\tag{1}$$

The vector $\mathbf{R}$ results from the Fourier transform $\mathscr{F}$ of the bridge girder motion vector $\mathbf{r}$ (the self-excited forces acting on cables and pylons are neglected here), where y, z and θ denote lateral, vertical and torsional displacements, respectively (Fig. 1). In Eq. (1), $\widetilde{K}=\omega B/\widetilde{V}$ represents the slowly-varying reduced frequency, where $\omega=2\pi f$ is the circular frequency of the motion, B is the bridge deck width, $V(t)=\sqrt{[V_m+u(t)]^2+w^2(t)}$ is the time-varying wind velocity magnitude, V_m is the mean wind speed, while $u(t)$ and $w(t)$ are the longitudinal and vertical turbulent wind fluctuations, respectively; $\widetilde{\alpha}$ denotes the slowly-varying angle of attack, where $\alpha(t)=\text{atan}\{w(t)/[V_m+u(t)]\}$. The aerodynamic derivatives determine the transfer function $\mathbf{G}(\widetilde{K},\widetilde{\alpha})$ as explained in Barni et al. (2021).

Aiming at a time-domain description of the self-excited forces, the transfer function can be approximated by Roger's rational function (Roger, 1977):

$$\mathbf{G}(\widetilde{K},\widetilde{\alpha})=\frac{1}{2}\rho\widetilde{V}^2\left(\mathbf{A}_1(\widetilde{\alpha})+\mathbf{A}_2(\widetilde{\alpha})i\widetilde{K}+\sum_{l=1}^{N-2}\mathbf{A}_{l+2}(\widetilde{\alpha})\frac{i\widetilde{K}}{i\widetilde{K}+d_l(\widetilde{\alpha})}\right)\tag{2}$$

Here, ρ is the air density, $N-2$ is the number of additional aeroelastic states; $\mathbf{A}_l(\widetilde{\alpha})\in\mathbb{R}^{3\times3}$ and $d_l(\widetilde{\alpha})\in\mathbb{R}^+$ are the time-variant rational-approximation coefficients, determined from the aerodynamic derivatives through a nonlinear least-squares fitting, as discussed in Barni et al. (2021). The multivariate rational function approximation can be visualised as a surface, and the model is therefore called 2D RFA model. Taking the inverse Fourier transform of Eq. (2), considering $\mathbf{A}_l$ and d_l as frozen-time functions of the angle of attack, one obtains the following expression of the self-excited forces:

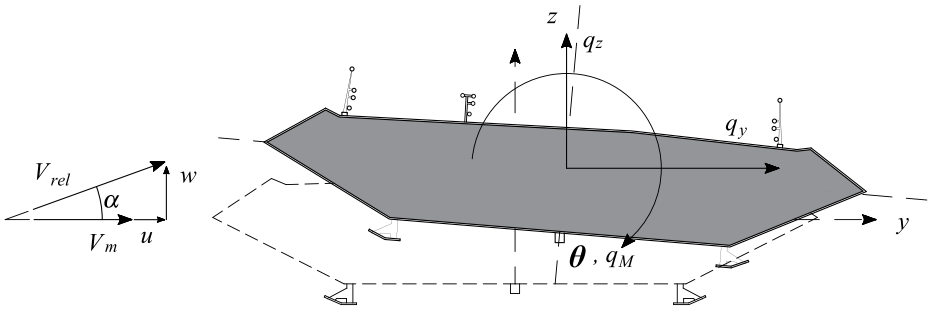

Fig. 1. Sketch of the Hardanger Bridge section with the reference system for displacements, forces and wind velocities.

$$\mathbf{q}_{se}(t,\widetilde{\alpha})=\frac{1}{2}\rho\widetilde{V}^2\left[\mathbf{A}_1(\widetilde{\alpha})\mathbf{r}(t)+\frac{B}{\widetilde{V}}\mathbf{A}_2(\widetilde{\alpha})\dot{\mathbf{r}}(t)+\sum_{l=1}^{N-2}\mathbf{A}_{l+3}(\widetilde{\alpha})\,\boldsymbol{\lambda}_l(t)\right] \tag{3}$$

$\boldsymbol{\lambda}_l \in \mathbb{R}^{3\times 1}$ are the additional aeroelastic states, which can be obtained from:

$$\dot{\boldsymbol{\lambda}}_l = -d_l(\widetilde{\alpha})\frac{\widetilde{V}}{B}\,\boldsymbol{\lambda}_l + \dot{\mathbf{r}} \tag{4}$$

This time-variant self-excited force model can be extended to the case of a three-dimensional linearised bridge structure, characterised by N_{mod} vibration modes and exposed to a partially-correlated random wind field, in a similar way to Barni et al. (2022). Since the turbulent wind field varies in both space and time, wind velocity magnitude and angle of attack also change along the bridge girder ($\widetilde{V}(x,t)$, $\widetilde{\alpha}(x,t)$, where x denotes the bridge girder longitudinal axis). By carrying out a modal analysis of the suspension bridge in the neighbourhood of the deformed configuration under self-weight (or self-weight and mean wind load), the nodal displacement vector $\mathbf{r}$ can be expressed as the sum of the products of the selected natural mode shapes, $\boldsymbol{\varphi}_i(x) = [\varphi_{iy}(x) \quad \varphi_{iz}(x) \quad \varphi_{i\theta}(x)]^T$, and the corresponding generalised coordinates, $\boldsymbol{\eta}_i(t)$ [$\mathbf{r}(x,t) = \boldsymbol{\Phi}(x)\boldsymbol{\eta}(t)$]. Then, the bridge equation of motion can be written in the modal space, yielding:

$$\begin{aligned}\ddot{\boldsymbol{\eta}} &= -\widehat{\mathbf{M}}^{-1}[\widehat{\mathbf{C}}+\widehat{\mathbf{C}}_{ae}(\widetilde{\alpha})]\dot{\boldsymbol{\eta}} - \widehat{\mathbf{M}}^{-1}[\widehat{\mathbf{K}}+\widehat{\mathbf{K}}_{ae}(\widetilde{\alpha})]\boldsymbol{\eta}\\ &+\frac{1}{2}\rho\,\widehat{\mathbf{M}}^{-1}\int_{\ell}\boldsymbol{\Phi}^T\widetilde{V}^2\left[\sum_{l=1}^{N-2}\mathbf{A}_{l+2}(\widetilde{\alpha})\,\boldsymbol{\psi}_l\right]dx+\widehat{\mathbf{q}}_{ext}\end{aligned} \tag{5}$$

where

$$\widehat{\mathbf{C}}_{ae} = -\frac{1}{2}\rho B\int_{\ell}\boldsymbol{\Phi}^T\,\widetilde{V}\,\mathbf{A}_2(\widetilde{\alpha})\,\boldsymbol{\Phi}\,dx \in \mathbb{R}^{N_{mod}\times N_{mod}}$$

$$\widehat{\mathbf{K}}_{ae} = -\frac{1}{2}\rho\int_{\ell}\boldsymbol{\Phi}^T\,\widetilde{V}^2\,\mathbf{A}_1(\widetilde{\alpha})\,\boldsymbol{\Phi}\,dx \in \mathbb{R}^{N_{mod}\times N_{mod}}$$

$\widehat{\mathbf{M}}, \widehat{\mathbf{C}}$ and $\widehat{\mathbf{K}} \in \mathbb{R}^{N_{mod}\times N_{mod}}$ represent the structural mass, damping and stiffness matrices, respectively, in generalised coordinates, while $\widehat{\mathbf{C}}_{ae}$ and $\widehat{\mathbf{K}}_{ae}$ represent a part of the generalised aerodynamic damping and stiffness matrices (another contribution comes from the additional aeroelastic states); ℓ indicates that the integral is extended over the entire length of the bridge deck. The external load vector $\widehat{\mathbf{q}}_{ext}$, here projected onto the modal space, can be obtained through a dynamic linearisation around the slowly-varying angle of attack, as explained in Barni et al. (2022). Then, a state-space transformation can be applied, posing $\boldsymbol{\gamma}_1 = \boldsymbol{\eta}$, $\boldsymbol{\gamma}_2 = \dot{\boldsymbol{\eta}}$ and $\boldsymbol{\gamma}_{l+2} = \boldsymbol{\lambda}_l$, $l \in \{1,2,\ldots,N-2\}$, and the integral in Eq. (5) can be expressed as the product of a block matrix $\mathbf{Q}_{ad}(\widetilde{V},\widetilde{\alpha})$ and a column vector $\boldsymbol{\gamma}_{ad}$, which includes all the additional aeroelastic states $\boldsymbol{\gamma}_{ad}(t) = [\boldsymbol{\gamma}_3(x_1,t) \quad \cdots \quad \boldsymbol{\gamma}_N(x_1,t) \quad \cdots \quad \boldsymbol{\gamma}_3(x_{N_x},t) \quad \cdots \quad \boldsymbol{\gamma}_N(x_{N_x},t)]^T \in \mathbb{R}^{3\cdot(N-2)\cdot N_x}$, where N_x denotes the number of nodes (identified by the coordinates $x_1,\ldots,x_{N_x}$) used to discretise the bridge girder (see Barni et al., 2022 for more details). Eqs. (3), (4), (5) can thus be written as a linear time-variant state-space model:

$$\begin{bmatrix}\dot{\boldsymbol{\gamma}}_1\\ \dot{\boldsymbol{\gamma}}_2\\ \dot{\boldsymbol{\gamma}}_{ad}\end{bmatrix} = \begin{bmatrix}\mathbf{0} & \mathbf{I} & \mathbf{0}\\ -\widehat{\mathbf{M}}^{-1}(\widehat{\mathbf{K}}+\widehat{\mathbf{K}}_{ae}) & -\widehat{\mathbf{M}}^{-1}(\widehat{\mathbf{C}}+\widehat{\mathbf{C}}_{ae}) & \widehat{\mathbf{M}}^{-1}\mathbf{Q}_{ad}\\ \mathbf{0} & \boldsymbol{\Xi} & \mathbf{G}_{ad}\end{bmatrix}\begin{bmatrix}\boldsymbol{\gamma}_1\\ \boldsymbol{\gamma}_2\\ \boldsymbol{\gamma}_{ad}\end{bmatrix} + \begin{bmatrix}\mathbf{0}\\ \widehat{\mathbf{M}}^{-1}\widehat{\mathbf{q}}_{ext}\\ \mathbf{0}\end{bmatrix} \tag{6}$$

where:

$$\mathbf{Q}_{ad}\left(\widetilde{V},\widetilde{\alpha}\right) = \frac{1}{2}\rho\,\Delta x[\ \mathbf{Z}(x_1,\widetilde{\alpha}(x_1)) \quad \cdots \quad \mathbf{Z}(x_k,\widetilde{\alpha}(x_k))\ ] \in \mathbb{R}^{N_{mod}\times[3\cdot(N-2)\cdot N_x]}$$

$$\mathbf{Z}(x_k,\widetilde{\alpha}(x_k)) = \left[\boldsymbol{\Phi}(x_k)^T\left[\mathbf{A}_3(\widetilde{\alpha}(x_k))\widetilde{V}^2(x_k)\right] \quad \cdots \quad \boldsymbol{\Phi}(x_k)^T\left[\mathbf{A}_N(\widetilde{\alpha}(x_k))\widetilde{V}^2(x_k)\right]\right] \in \mathbb{R}^{N_{mod}\times[3\cdot(N-2)]}$$

$$\mathbf{G}_{ad}\left(\widetilde{V},\widetilde{\alpha}\right) = -B^{-1}\begin{bmatrix}\mathbf{D}(x_1,t) & & \\ & \ddots & \\ & & \mathbf{D}(x_{N_x},t)\end{bmatrix} \in \mathbb{R}^{[3\cdot(N-2)\cdot N_x]\times[3\cdot(N-2)\cdot N_x]}$$

$$\mathbf{D}(\widetilde{\alpha}(x_k),t) = \begin{bmatrix}d_1(\widetilde{\alpha}(x_k,t))\,\mathbf{I}\,\widetilde{V}(x_k,t) & & \\ & \ddots & \\ & & d_{N-2}(\widetilde{\alpha}(x_k,t))\,\mathbf{I}\,\widetilde{V}(x_k,t)\end{bmatrix} \in \mathbb{R}^{[3\cdot(N-2)\cdot N_x]\times[3\cdot(N-2)]}$$

$$\boldsymbol{\Xi} = \begin{bmatrix}\left.\begin{matrix}\boldsymbol{\Phi}(x_1)\\ \vdots\\ \boldsymbol{\Phi}(x_{N_x})\end{matrix}\right\}N-2\text{ times}\\ \vdots\end{bmatrix} \in \mathbb{R}^{[3\cdot(N-2)\cdot N_x]\times N_{mod}}$$

$\mathbf{I} \in \mathbb{R}^{N_{mod}\times N_{mod}}$ is the identity matrix, and Δx is the spanwise distance between the nodes (assumed here as equispaced). In compact form, one can write:

$$\dot{\boldsymbol{\gamma}}(t) = \boldsymbol{\Omega}\left(\widetilde{V},\widetilde{\alpha}\right)\boldsymbol{\gamma}(t) + \mathbf{B}\widehat{\mathbf{q}}_{ext}(t) \tag{7}$$

$\mathbf{B} = \begin{bmatrix}\mathbf{0} & \widehat{\mathbf{M}}^{-1} & \mathbf{0}\end{bmatrix}^T \in \mathbb{R}^{[2N_{mod}+3\cdot(N-2)\cdot N_x]\times N_{mod}}$ is the input matrix, $\boldsymbol{\gamma} \in \mathbb{R}^{2\cdot N_{mod}+3\cdot(N-2)\cdot N_x}$ is the state vector, while $\boldsymbol{\Omega}\left(\widetilde{V},\widetilde{\alpha}\right) \in \mathbb{R}^{[2\cdot N_{mod}+3\cdot(N-2)\cdot N_x]\times[2\cdot N_{mod}+3\cdot(N-2)\cdot N_x]}$ is the slowly-varying time-variant state matrix. It is worth emphasising that the dependence of the state matrix in Eq. (7) on the local flow characteristics along the deck allows taking into account the effect of the partial correlation of the random wind field on the modulation of the self-excited forces due to large-scale oncoming turbulence.

The dynamic response of the bridge can efficiently be determined by transforming Eq. (7) into a discrete-time state-space equation, given the sampling rate $1/\Delta t$:

$$\boldsymbol{\gamma}(s+1) = \boldsymbol{\Omega}_d(s)\boldsymbol{\gamma}(s) + \mathbf{B}_d(s)\widehat{\mathbf{q}}_{ext}(s) \tag{8}$$

where:

$$\boldsymbol{\Omega}_d(s) = e^{\boldsymbol{\Omega}(s\Delta t)\Delta t} \quad ; \quad \mathbf{B}_d(s) = [\boldsymbol{\Omega}_d(s) - \mathbf{I}]\boldsymbol{\Omega}(s\Delta t) \tag{9)–(10}$$

s is an integer-valued variable (the discrete-time index), $\boldsymbol{\Omega}_d$ is the discrete-time state matrix, and $\mathbf{B}_d$ is the discrete-time input matrix.

It is worth emphasising that the governing differential equation (Eq. (7)) maintains a linear relationship between self-excited forces and bridge motion, but a nonlinear-like behaviour is introduced by the time-variant nature of the dynamic system. In contrast, when the aerodynamic derivatives exhibit a nonnegligible dependence on even small bridge vibration amplitude (for instance, in the case of bluff bridge cross sections, as discussed in Mannini et al., 2016) or in a post-critical flutter analysis, it is necessary to consider a fully nonlinear amplitude-

dependent model for self-excited forces (e.g., Gao et al., 2020; Skyvulstad et al., 2021; 2023). However, amplitude-dependent models do not allow the identification of a state matrix since the aerodynamic forces depend on the bridge response, resulting in computationally more expensive calculations, especially for a multi-degree-of-freedom problem like a suspension bridge. Moreover, a fully nonlinear approach is usually expected not to be necessary in precritical conditions for quasi-streamlined cross-sections, since an amplitude-dependence of the aerodynamic derivatives is often observed only for very large vibrations. On the other hand, the nonlinearity associated with the low-frequency contribution to the angle of attack of the bridge motion (background response) is usually small compared to the wind counterpart and can reasonably be neglected (Barni et al., 2022), although it would be straightforward to account for it through an iterative procedure (note that this may be very important in case of nonsynoptic winds). Finally, the framework reported above might also be used to determine the suspension bridge response under nonstationary winds. Indeed, a slowly-varying mean wind velocity and angle of attack are usually assumed to account for the transient effects of nonsynoptic winds (e.g., Chen, 2014; Hu et al., 2013).

Crucial points in all band-superposition approaches, and therefore also in the 2D RFA model, are the assumption of slow variations in the angle of attack and wind velocity magnitude compared to the motion of the bridge, and the choice of the cutoff frequency below which wind velocity fluctuations are assumed to be effective in modulating the self-excited forces. Concerning the former issue, the 2D RFA model has experimentally been validated under both multi-harmonic and broad-band random angle of attack for different bridge section geometries; a frequency ratio of the bridge motion to the modulating angle of attack as low as 1.7 has successfully been tested (Barni et al., 2021, 2023b; Barni, 2022). The second issue is clearly the major drawback of all band-superposition models, and the different methods followed in the literature are thoroughly discussed in Barni et al. (2022). In order to maximise the parametric effects of oncoming turbulence, a multiple cutoff strategy was proposed in Barni et al. (2022), setting a different cutoff frequency for the self-excited force components associated with lateral, vertical, and torsional motions. The same approach is used here, considering three distinct slowly-varying wind velocity magnitudes and angles of attack, denoted as $\widetilde{V}_y$, $\widetilde{V}_z$, $\widetilde{V}_\theta$, and $\widetilde{\alpha}_y$, $\widetilde{\alpha}_z$, $\widetilde{\alpha}_\theta$, which are determined by low-pass filtering with the cutoff at the first natural frequency of the corresponding first vibration modes. In this regard, it is important to remark that the equations presented above were written based on a single cutoff frequency for the sake of simplificty and conciseness. The adoption of multiple cutoff frequencies for the angle of attack requires some modifications in Eq. (6) and in particular in the construction of the matrices $\mathbf{G}_{ad}$ and $\mathbf{D}$, as explained in details in Barni et al. (2022). Similar straightforward changes must be introduced for the slowly-varying wind velocity magnitude in the matrices $\mathbf{Q}_{ad}$ and $\mathbf{D}$. It is also important to note that the variation in the 2D RFA coefficients with both $\widetilde{V}$ and $\widetilde{\alpha}$ is directly accounted for in physical coordinates before modal projection (see Eqs. (3) and (4)). This implies that the slowly-varying turbulence parameters obtained through low-pass filtering modulate each modal component in a consistent manner, namely the same cutoff frequencies are applied to the lateral, vertical and torsional components of all modes (see also the extensive discussion in Barni et al., 2022 about the role of multiple cutoffs with respect to mode coupling effects). Finally, the actual impact of the cutoffs on the results for the considered case study will be further discussed at the end of this paper by finally ignoring the assumption of slow-variation in the wind angle of attack and simply removing them.

3. Methodologies

3.1. Monte Carlo approach

Generally, for a time-invariant system, the asymptotic flutter stability threshold is governed by the sign of the real part of the state matrix eigenvalues. In contrast, such eigenvalues vary with time for a time-variant stochastic system such as that described by Eq. (7), thus leading to more complicated concepts of stability, such as sample or p-th moment stability (e.g., Arnold et al., 1984; 1986). Lin and Ariaratnam (1980) and later Bucher and Lin (1988a) studied the sample stability of a similar problem by analysing the behaviour of the statistical moments. This approach was allowed by considering turbulence as a white-noise process that only affects the wind kinetic pressure in the self-excited force formulation, thus neglecting changes in the indicial function. Under these assumptions, the turbulence parametric excitation can be assimilated to a Wiener process (Xie, 2006) and the bridge response to a Markov vector, inheriting all the good properties for the stability of Itô-type stochastic differential equations.

In contrast, the problem described in Eq. (7) is much more complicated, aiming to consider all parametric effects of large-scale turbulence. It may be possible to express the slowly-varying parameters $\widetilde{\alpha}$ and $\widetilde{V}$ from scalar Wiener processes, as the output of autoregressive filters (e.g., Bartoli et al., 1997; Caracoglia, 2013), and then include them in Eq. (6) as additional states (state augmentation, see Grigoriu, 2002). This would result in a nonlinear Itô stochastic differential equation, the stability of which could be formally investigated through the numerical assessment of Lyapunov exponents (for sample stability) or moment Lyapunov exponents (for p-th moment stability). This approach may be explored in a future study. In contrast, in this work the influence of realistic turbulence on the stability threshold is simply assessed by determining in a heuristic and approximate, yet unequivocal way the position of the vertical asymptote of the nonlinear buffeting response curves. The bridge dynamic response is obtained using a Monte Carlo approach in a similar way to Barni et al. (2022). The turbulent random wind field, necessary to obtain the external buffeting forces, $\widehat{\mathbf{q}}_{ext}$, as well as the slowly-varying wind velocity magnitude and angle of attack, is generated through the method of Shinozuka and Jan (1972) for different turbulence intensities and integral length scales. For the sake of simplicity, the wind-induced static rotation of the bridge deck is disregarded in the present analysis. This rotation is approximately 0.7 deg at midspan for a wind speed of 65 m/s, which, although non-negligible, is relatively small compared to the mean wind inclination of 2.5 deg (furthermore, the latter is constant along the bridge girder).

3.2. Floquet multipliers

The previous approach allows considering the full effect of parametric excitation caused by large-scale turbulence, but it does not help much understand the mechanisms standing behind the variation in the flutter stability threshold. For this reason, the problem is simplified by considering a sinusoidal gust with period T^*; then, the stability of the time-variant system described by Eq. (7) is addressed travelling the periodic trajectory drawn by either the slowly-varying wind velocity magnitude or the slowly-varying angle of attack:

$$\widetilde{V}(t) = V_m + V_0 \sin\left(\frac{2\pi t}{T^*}\right) \; ; \; \widetilde{\alpha}(t) = \alpha_m + \alpha_0 \sin\left(\frac{2\pi t}{T^*}\right) \tag{12}$$

Since the stability of a linear time-variant system only depends on the time-variant state matrix, the input term $\mathbf{B}\widehat{\mathbf{q}}_{ext}$ in Eq. (7) can be ignored in this analysis. The solution of the autonomous part of Eq. (7) can be expressed as follows:

$$\boldsymbol{\gamma}(t) = \boldsymbol{\Phi}_{\boldsymbol{\Omega}}(t, t_0)\boldsymbol{\gamma}(t_0) \tag{13}$$

where t_0 denotes the initial time, and $\boldsymbol{\Phi}_{\boldsymbol{\Omega}}(t, t_0) \in \mathbb{R}^{n\times n}$ ($n = 2{\cdot}N_{mod} + 3{\cdot}(N-2){\cdot}N_x$) is the state-transition matrix associated with the state matrix $\boldsymbol{\Omega}\left(\widetilde{V}, \widetilde{\alpha}\right)$, which solves the following differential equation:

$$\dot{\mathbf{\Phi}}_{\mathbf{\Omega}}(t,t_0) = \mathbf{\Omega}\left(\widetilde{V},\widetilde{\alpha}\right)\mathbf{\Phi}_{\mathbf{\Omega}}(t,t_0)$$
$$\mathbf{\Phi}_{\mathbf{\Omega}}(t_0,t_0) = \mathbf{I} \in \mathbb{R}^{n\times n} \tag{14}$$

Given the obvious periodicity of the state matrix, Floquet's theory (e.g., Richards, 1983) tells that the eigenvalues of the monodromy matrix $\mathbf{\Phi}_{\mathbf{\Omega}}(T^*,0)$, the so-called Floquet multipliers ς_j, rule the system stability; indeed, a linear time-periodic system is stable if and only if $|\varsigma_j| \leq 1, \forall j$ (see Appendix A for further explanations).

Based on the assumed sinusoidal form of the slowly-varying angle of attack and wind velocity magnitude, the equation governing the bridge dynamics (Eq. (7)) belongs to the family of Hill's equations, where the parametric excitation can be expressed as a Fourier series with fundamental period T^*. Indeed, the nonlinear relation between the aerodynamic derivatives and the slowly-varying reduced frequency and above all angle of attack, accounted for by the 2D RFA model, gives rise to a multi-harmonic parametric excitation. Consequently, these systems can exhibit parametric resonances corresponding to higher-order harmonics (e.g., Ying et al., 2019), as will be apparent in Section 5.2.

4. Case study

4.1. Hardanger Bridge

The model previously introduced is used to study the stability of the Hardanger Bridge in turbulent flow. This suspension bridge crosses the Hardanger Fjord, in Norway, and is characterised by a 1310 m-long main span and two 186 m-high reinforced concrete towers. It is the largest Norwegian bridge (the third in Europe). The girder is a 3.2 m-high and 18.3 m-wide single-box steel deck (Fig. 1) composed of orthotropic plates. The bridge finite element model is the same used in Barni et al. (2022). The modal analysis was performed after applying the dead load, accounting for the geometrically nonlinear stiffness provided by the cables. Based on previous analyses, buffeting and stability calculations are performed considering 13 modes (1–7, 12 to 15, and 17, reported in Table 1). A structural modal damping ratio of 0.5% is considered for all modes. In light of the modal characteristics of the bridge, the cutoff frequencies for the three motion components, which define the slowly-varying wind angles of attack and wind velocity magnitudes, are $f_y^c = 0.05$ Hz, $f_z^c = 0.11$ Hz, and $f_\theta^c = 0.36$ Hz.

4.2. Aerodynamic coefficients

The aerodynamic derivatives, which were measured for different mean angles of attack with forced vibration tests and reported in Barni et al. (2021), are here approximated with 2D rational functions consisting of $N = 4$ terms (two additional aeroelastic states), adopting 5th-order polynomials for all $\mathbf{A}_i$, $i = 1,\ldots,N$, and d_l, $l = 1,\ldots,N-2$, parameters (see Eqs. (3) and (4)). Therefore, 228 coefficients are determined, ensuring high accuracy in the experimental data fitting (see Fig. 2). The 2D RFA approximation is carried out considering 11 angles of attack (namely, −8, −6, −4, −2, 0, 1, 2, 4, 5, 6, 7 and 8 deg) in a reduced velocity ($V_r = V_m/(fB)$) range up to 55. In the calculations, when the slowly-varying angle of attack $\widetilde{\alpha}$ falls outside this range, the 2D RFA coefficients are kept equal to the values corresponding to either −8 or +8 deg. Some experimental aerodynamic derivatives associated with the torsional motion are reported in Fig. 2 for a subset of angles of attack, together with the corresponding section traces of the 2D rational function approximation surface. Two essential features must be underlined in Fig. 2. First, the aerodynamic coefficients show a strong dependence on the mean angle of attack, which implies a possible marked time-variant behaviour of the dynamic system. Secondly, the important coefficient A_2^*, which is directly related to the aerodynamic damping in torsion, takes positive values (i.e., the attendant aerodynamic damping contribution becomes negative) for mean angles of attack larger than about 5 deg. This feature clearly emphasises the importance of a model that accounts for such a nonlinearity. Finally, it is important to note that the aerodynamic effects of small-scale turbulence may also be considered by determining the 2D RFA coefficients from a set of aerodynamic derivatives measured in a specifically designed small-scale turbulent flow (see, e.g., Lander and Letchford, 2023).

Table 1
Overview of the vibration modes of the Hardanger Bridge considered in the analyses.

Mode	Frequency [Hz]	Antinodes	Dominant motion
1	0.050	1	Symmetric lateral
2	0.098	2	Antisymmetric lateral
3	0.110	2	Antisymmetric vertical
4	0.140	3	Symmetric vertical
5	0.169	3	Symmetric lateral
6	0.197	2	Symmetric vertical
7	0.210	4	Antisymmetric vertical
12	0.272	5	Symmetric vertical
13	0.283	4	Antisymmetric lateral
14	0.330	6	Antisymmetric vertical
15	0.360	1	Symmetric torsional
17	0.392	5	Symmetric lateral and torsional

4.3. Turbulent wind field characteristics

Various random wind fields are generated for the Monte Carlo analyses devised in Section 3.1. Specifically, the longitudinal turbulence intensity I_u and integral length scale L_u are assumed to vary between 10% and 25% and between 100 m and 300 m, respectively. These ranges are chosen based on the typical values of interest for these parameters in the case of long-span suspension bridges similar to the Hardanger Bridge. The vertical turbulence intensity and integral length scale are set to half and 10% of their longitudinal counterparts, respectively. Two-point normalised cross-spectra in the classical Davenport's form (Davenport, 1962) are assumed with decay coefficients equal to 10 and 6.5 for the longitudinal and vertical velocities, respectively. The turbulent wind velocity components are generated as 1 h-long time series at a sampling rate of 6 Hz for 100 equally-spaced points along the bridge girder ($\Delta x = 13.23$ m). 20 random wind field samples are considered for each (I_u, L_u) pair. According to the wind field measurements reported in Fenerci and Øiseth (2017) and Fenerci and Øiseth (2018), an upward inclination of the mean wind velocity between 2 and 2.5 deg with respect to the horizontal plane can normally be observed in the Hardanger Bridge site. For this reason, a mean angle of attack $\alpha_m = 2.5$ deg is considered herein for the baseline calculations.

In the time-periodic system analyses presented in Section 3.2, in analogy with the broad-band parametric excitation, a range of pumping frequencies ($f^* = 1/T^*$) between 0.01 and 0.36 Hz (with a step of 0.001 Hz) is considered, being 0.36 Hz the still-air natural frequency of the first torsional vibration mode. Nevertheless, according to the multiple cutoff frequency approach, the sinusoidal variation in $\widetilde{V}_y$, $\widetilde{V}_z$, $\widetilde{V}_\theta$, $\widetilde{\alpha}_y$, $\widetilde{\alpha}_z$ and $\widetilde{\alpha}_\theta$ is considered only up to the corresponding cutoff frequency (only the mean values V_m and α_m are retained beyond it). This guarantees the validity of the basic assumption of slow variation in the parametric excitation with respect to the bridge motion. In terms of intensity, the wind velocity amplitude (V_0) is varied between 1% and 50% (with steps of 1%) of V_m, while the angle of attack amplitude (α_0) between 0 and 10 deg (with steps of 0.1 deg).

5. Results

5.1. Stability under broad-band turbulence

Considering the aerodynamic derivatives for a mean wind inclination of 2.5 deg, according to the classical deterministic calculation, the flutter critical wind speed is $V_{cr} = 65.1$ m/s, and the critical frequency is

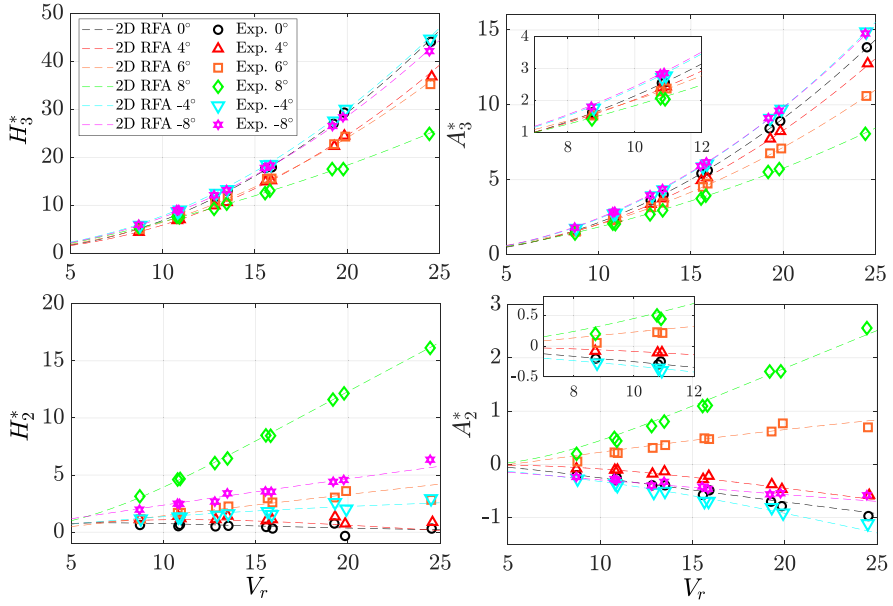

Fig. 2. Lift and moment aerodynamic derivatives associated with the torsional motion for the Hardanger Bridge (see also Barni et al., 2021). Results of wind tunnel measurements are reported as a function of the reduced wind velocity V_r for various mean angles of attack. 2D RFA approximations are also shown.

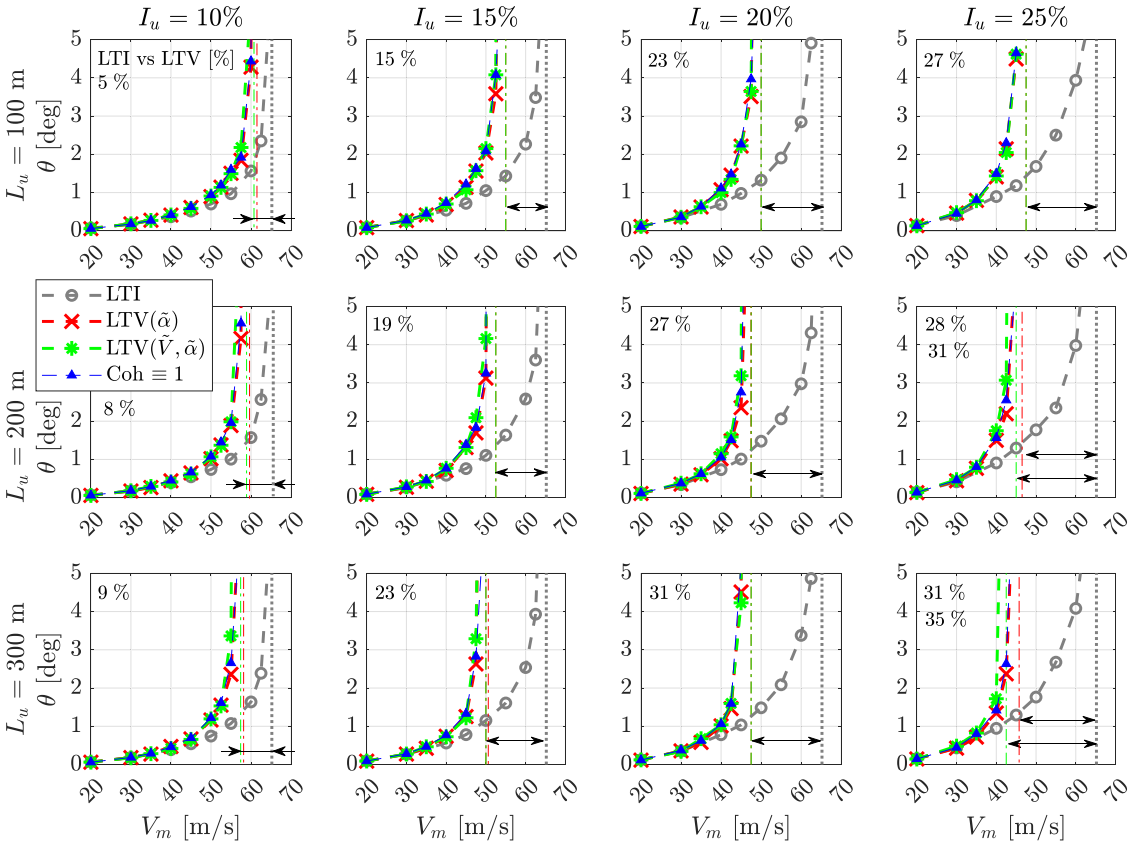

Fig. 3. RMS of mid-span nonlinear buffeting torsional response of the Hardanger Bridge obtained according to either a linear time-invariant (grey circles) or a linear time-variant (red crosses if only the slowly-varying angle of attack $\tilde{\alpha}$ is considered; green asterisks if both $\tilde{\alpha}$ and $\tilde{V}$ are taken into account) formulation of the self-excited forces. The percentages in the top-left corner of each frame indicates the differences between the LTI and LTV flutter threshold. Finally, the blue lines with filled triangular markers denote the LTV results obtained assuming a perfectly-correlated parametric variation in the slowly-varying angle of attack (Coh $\equiv 1$).

f_{cr}= 0.297 Hz. This result might also be obtained by imposing $\widetilde{V}(t) \equiv V_m$ and $\widetilde{\alpha}(t) \equiv 2.5$ deg in Eq. (7), yielding the so-called linear time-invariant (LTI) system. Fig. 3 compares the linear time-invariant and the linear time-variant (LTV) torsional response of the bridge for different turbulent wind fields, in terms of root-mean-square (RMS) of the rotations. Specifically, the mean of the 20 RMS values for each simulated 1 h-long random wind field are shown in the figure. The standard deviation of these RMS values is always small, except, as expected, very close to the flutter stability threshold; therefore, it does not significantly affect the buffeting response patterns and the estimated stability limits. The red crosses account only for the parametric effect of the slow variation in the angle of attack, while the green asterisks also consider the fluctuations of kinetic pressure and reduced wind velocity. Since here the focus is mainly on the stability threshold, lateral and vertical responses are not reported for the sake of brevity. Fig. 3 clearly shows that the flutter stability of the Hardanger Bridge is systematically lowered by the random parametric effects of turbulence. In particular, the most destabilising contribution comes from the angle of attack variation. A non-negligible, though minor, role of $\widetilde{V}$ can be observed only for turbulence intensities and integral length scales higher than 20% and 200 m, respectively. It is worth emphasasing that this conclusion would not significantly change if one removed the cutoffs, also considering the parametric excitation at twice the natural frequencies (though violating the underlying basic assumption of the 2D RFA model). Fig. 4 shows the bridge response spectra corresponding to two representative points near the instability onset of the RMS-curves in Fig. 3. The results confirm that in this case the time-variant modelling of self-excited forces mainly affects the bridge torsional response (Barni et al., 2021, 2022) although, due to the aerodynamic coupling, a significant torsional mode contribution also appears in the lateral and even more in the vertical response of the bridge deck. In particular, the parametric excitation due to the slowly-varying angle of attack leads to a higher and sharper peak associated with the first torsional natural frequency, which reflects a damping reduction. In contrast, the parametric effect of wind velocity magnitude fluctuations only widens the peaks corresponding to the unstable mode. This seems to be due to the torsional aerodynamic stiffness (mainly related to the aerodynamic derivative A_3^*), which makes the torsional mode frequency slightly vary in time as a result of fluctuations of $\widetilde{V}$, spreading the resonance response around the linear time-invariant value. Though not reported in Fig. 3 in the interest of clarity, calculations for a turbulence intensity $I_u = 5\%$ showed nearly negligible time-variant effects in such a low-turbulence condition.

In Barni et al. (2022), the loss of stability of the Hardanger Bridge was ascribed, at least partly, to the variation over time in the torsional aerodynamic damping associated with the aerodynamic derivative A_2^*. Indeed, an unstable behaviour is promoted by a slowly-varying angle of attack when this becomes larger than about 5 deg (see Fig. 2), leading to positive values of A_2^* (negative contribution to the aerodynamic damping in torsion). In particular, if one considers as an example a mean wind speed of 45 m/s (corresponding to a reduced velocity for the torsional motion of about 7.5), in the worst case of I_u= 25% and L_u= 300 m, turbulence-induced fluctuations in the reduced velocity can produce a maximum variation of A_2^* of about ± 70% (around the value associated with the mean wind velocity and the mean angle of attack of 2.5 deg). In the same wind conditions, changes in the angle of attack lead to variations of A_2^* between −50% and +135%. As explained better in Section 5, this argument suggests the different impact on bridge stability of these two parametric effects. It also makes plausible the monotonic stability reduction with the turbulence intensity, since a higher I_u means higher fluctuations of $\widetilde{V}$ and $\widetilde{\alpha}$. In contrast, when a larger integral length scale of turbulence is considered, the power associated with low-frequency

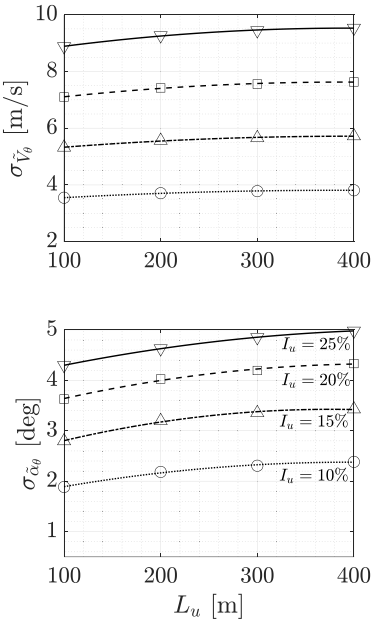

Fig. 5. RMS of the slowly-varying wind velocity magnitude and angle of attack associated with the torsional cutoff frequency for different longitudinal turbulence intensities and integral length scales (the mean wind speed is always 40 m/s).

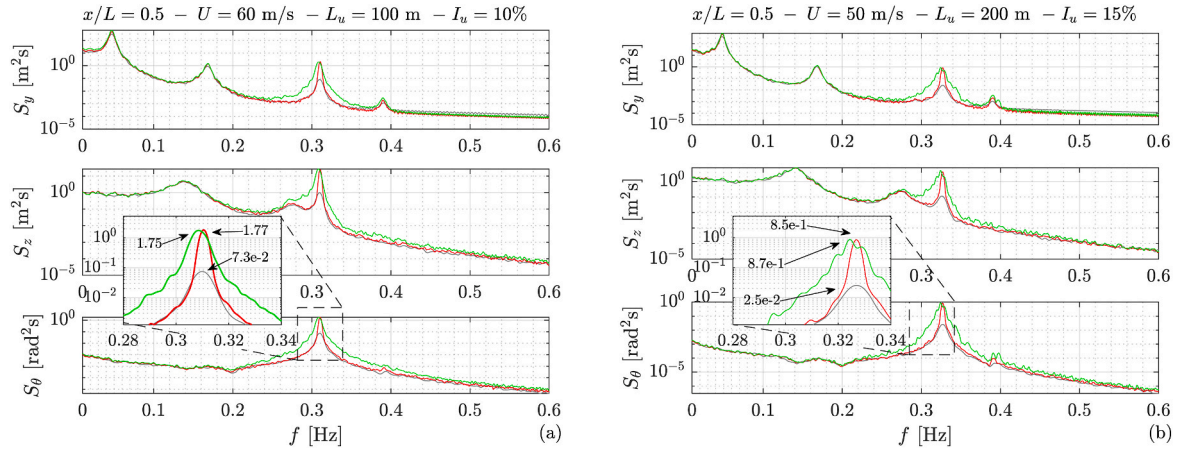

Fig. 4. Comparison of power spectral densities of lateral, vertical and torsional response for the mid-span bridge section obtained according to either a linear time-invariant (grey line) or a linear time-variant (red line: only slowly-varying $\widetilde{\alpha}$; green line: both $\widetilde{\alpha}$ and $\widetilde{V}$) formulation of the self-excited forces.

velocity fluctuations increases, and so does the variance of $\widetilde{V}$ and $\widetilde{\alpha}$, thus further reducing the system stability. However, the destabilising influence of the integral length scale of turbulence tends to saturate for large values of L_u. This is because, for $L_u \geq 300$ m, most of the turbulent kinetic energy is already encompassed below the cutoff frequency, and additional increases in the variance of the slowly-varying wind velocity magnitude and angle of attack become negligible when L_u gets larger, as clearly shown in Fig. 5.

Fig. 3 also reports the torsional response of the bridge to turbulent wind in a scenario of perfectly-correlated parametric variation in the angle of attack (though the external buffeting force $\widehat{\mathbf{q}}_{ext}$ in Eq. (7) remains partially correlated along the bridge girder). Surprisingly, the response curves essentially overlap with the previous ones, thus indicating a negligible effect of the spanwise correlation of the parametric excitation on the flutter instability mechanism and buffeting response. This counterintuitive result contradicts expectations outlined in previous works (e.g., Chen and Kareem, 2003; Barni et al., 2022) and will be explained in Section 6.

Finally, It is worth emphasising that, for all mean angles of attack considered, the aerodynamic derivatives of the Hardanger Bridge do not exhibit any amplitude-dependence at least up to rotations of 2 deg (Barni et al., 2021). Some nonlinear effects associated with oscillation amplitude might manifest for a larger torsional response; nevertheless, in line with previous works on a similar topic (e.g., Chen and Kareem, 2003; Diana et al., 2013; Diana and Omarini, 2020; Barni et al., 2022), it seems reasonable here to disregard this complication as the focus of the investigation is just on the bridge precritical response and flutter stability threshold.

5.2. Parametric effects of sinusoidal gusts

This section is instrumental in uncovering the reasons for the significant variation in the flutter stability threshold and buffeting response induced by large-scale turbulence and discussed in the preceding section. Although it may be conjectured that this destabilising effect is linked to the modulation of aerodynamic damping by turbulence (Barni et al., 2022), the actual mechanisms responsible for this loss of stability have not been clarified yet. For example, are parametric resonances the primary driver of destabilisation, or are there other mechanisms influencing the phenomenon? Does the parametric variation in aerodynamic stiffness play a role similar to what is seen in a Mathieu equation (Nayfeh and Mook, 2008)? Why does the spanwise coherence of the parametric excitation not seem to play a significant role in destabilising the system? To answer these questions, here the problem is tackled by representing turbulence as a time-periodic process, as outlined in Section 3.2. Indeed, this approach not only facilitates the formal definition of stability boundaries but also offers an insight into the various parametric excitation mechanisms.

Fig. 6 shows the evolution of the flutter stability threshold through curves (one for each mean wind velocity considered) that represent the amplitude and frequency of the parametric excitation for which a Floquet multiplier crosses the unit circle $\left(\max_j \left[\left|\varsigma_j(\alpha_0, \bar{f}^*)\right|\right] = 1\right)$. The reported stability charts refer to a sinusoidal gust periodically changing the angle of attack, considering either a constant mean wind inclination $\alpha_m = 2.5$ deg [Fig. 6(a)] or a horizontal mean wind field, $\alpha_m = 0$ deg [Fig. 6(b)]. The second scenario is instrumental in highlighting the possible role played by the mean angle of attack. When a sinusoidal gust amplitude and frequency pair lies above the stability boundary, the bridge response diverges to infinity at a rate equal to the maximum real part of the Floquet exponents (see Appendix A). In general, the system stability is reduced compared to the time-invariant scenario ($V_{cr}^{LTI} = 65.1$ or 65.2 m/s for $\alpha_m = 2.5$ deg and 0 deg, respectively) depending on the amplitude and frequency of the sinusoidal gust. Typical features of parametrically excited systems are evident, such as parametric resonances occurring at rational multiples of the frequency $f_\theta^{(15)}$ of the torsional mode, which drives the instability (since this is the only torsional mode visible in the charts, it will hereafter be referred to as f_θ). The primary resonance is visible in Fig. 6 as a wide pit in the chart boundaries for mean wind velocities of 35 and 40 m/s in Fig. 6(a), and 35 and 40 and 45 m/s in Fig. 6(b) (top-right corner of both figures). Though at higher mean wind speeds, analogous stability boundaries are obtained even if only the torsional mode is considered, thus demonstrating that these parametric resonances are only indirectly influenced by mode coupling. Furthermore, in the close neighbourhood of the torsional frequency a deep and narrow pit superposes to the wider and smoother pattern of the stability boundaries. This feature is likely associated with the higher-order harmonics in the parametric excitation (see, e.g., Ying et al., 2019) due to the abovementioned nonlinear relationship between the 2D RFA model parameters and the sinusoidally-varying angle of attack. Some narrow and deep secondary resonances (Lin, 1996; Nayfeh and Mook, 2008) of the main torsional frequency can also be recognised, such as those around $2/3f_\theta$, $f_\theta/2$ and $f_\theta/3$. The influence of the aerodynamic stiffness in torsion is also apparent, as the torsional frequency progressively reduces when the mean wind velocity increases.

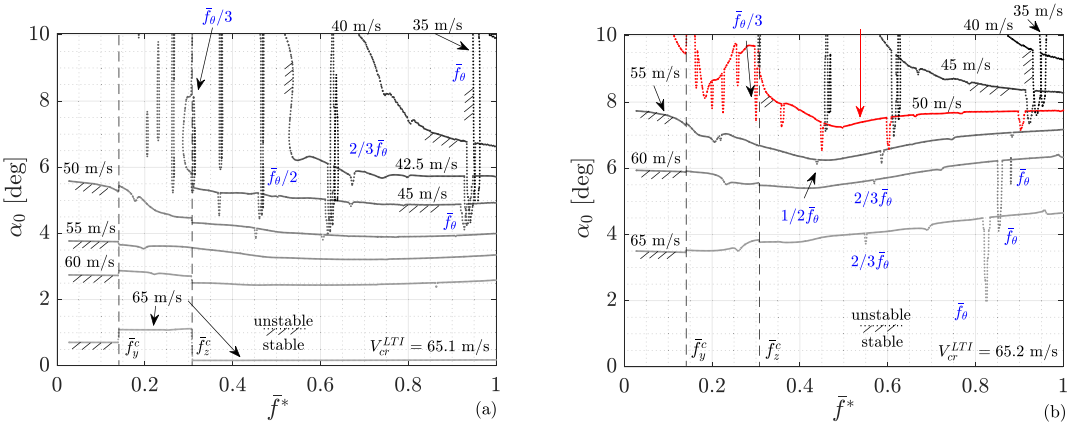

Fig. 6. Stability chart of the Hardanger Bridge for different amplitudes and frequencies of the perfectly correlated sinusoidal variation of the angle of attack modulating the self-excited forces, and for various mean wind speeds. V_{cr}^{LTI} represents the time-invariant flutter threshold. Results for (a) $\alpha_m = 2.5$ deg and (b) $\alpha_m = 0$ deg are shown. Frequencies are made dimensionless with the still-air frequency $f_{\theta,0}^{(15)}$: $\bar{f} = f/f_{\theta,0}^{(15)}$. $\bar{f}_y^c$ and $\bar{f}_z^c$ denote the cutoffs associated with lateral and vertical bridge motion components, respectively. The stability boundary highlighted in red is associated with the mean wind velocity considered in Fig. 8.

Another very important parametric effect is clear in Fig. 6, where nearly horizontal stability boundaries (i.e., independent of the pumping frequency) can often be encountered, especially for a mean angle of attack of 2.5 deg (Fig. 6(a)) and high mean wind velocities. This phenomenon is due to the nonlinear relationship between the aerodynamic derivatives and the angle of attack. Indeed, the average of the aerodynamic coefficients over a cycle of $\tilde{\alpha}$ is generally different from the coefficients evaluated at the mean angle of attack α_m, leading to mean aerodynamic stiffness and damping significantly different from the values assumed according to the classical time-invariant approach. This effect, which will be hereinafter called *average parametric effect*, can become important if the aerodynamic derivatives significantly vary with the mean angle of attack in a nonlinear and non-antisymmetric way around α_m. To better understand it, let consider a dynamical system described by a simple one-degree-of-freedom Hill-type differential equation with parametric damping and stiffness:

$$\ddot{x}+2\xi_0\omega_0[1-q\cdot g(\tilde{\alpha})]\dot{x}+\omega_0^2[1-q\cdot h(\tilde{\alpha})]x=0 \tag{15}$$

where q is a constant (mimicking, for instance, the wind kinetic pressure), while g and h are nonlinear and non-antisymmetric functions of the time-varying parameter $\tilde{\alpha}$, which play the same role as the parametric excitation in Eq. (5). To fix ideas, without loosing generality, let also assume that $\tilde{\alpha}$ sinusoidally oscillates around zero and $g(0)=h(0)=0$, so that ξ_0 and ω_0 directly represent the damping ratio and the circular frequency of the system for $\tilde{\alpha}\equiv 0$. In such a case, $\overline{g(\tilde{\alpha})}\neq g(\overline{\tilde{\alpha}})$ and $\overline{h(\tilde{\alpha})}\neq h(\overline{\tilde{\alpha}})$, where the overbar $\overline{(\cdot)}$ denotes the time-average operator. Then, if one defines the zero mean functions $g'(\tilde{\alpha})=g(\tilde{\alpha})-\overline{g(\tilde{\alpha})}$ and $h'(\tilde{\alpha})=h(\tilde{\alpha})-\overline{h(\tilde{\alpha})}$, Eq. (16) can be rewritten as follows:

$$\ddot{x}+2\xi_0\omega_0[1-q\cdot\overline{g(\tilde{\alpha})}-q\cdot g'(\tilde{\alpha})]\dot{x}+\omega_0^2[1-q\cdot\overline{h(\tilde{\alpha})}-q\cdot h'(\tilde{\alpha})] \tag{16}$$

This clearly results in time-invariant aerodynamic damping ($-2\xi_0\omega_0 q\,\overline{g(\tilde{\alpha})}$) and stiffness ($-q\omega_0^2\,\overline{h(\tilde{\alpha})}$) contributions, which leads to system instability when $\overline{g(\tilde{\alpha})}>1/q$. Clearly, such an effect is independent of the frequency of the parametric excitation. For the complex system described by Eq. (7), this effect is shown in Fig. 7 focusing on the aerodynamic coefficient $A_2^*(\tilde{\alpha})$, directly related to the aerodynamic damping in torsion. Here, the average of $A_2^*(\tilde{\alpha})$ around $\alpha_m=2.5$ deg grows and even becomes positive (negative contribution to the aerodynamic damping in torsion) as the parametric excitation amplitude and the mean wind velocity increase ($\alpha_0=0$ deg represents the LTI condition). Since A_2^* is less asymmetric around 0 deg, this effect is less pronounced in Fig. 7(b), where, moreover, the average of $A_2^*(\tilde{\alpha})$ only shows negative values. However, the average parametric effect associated with other aerodynamic derivatives is anyway able to destabilise the system (though at higher wind velocities), as shown in Fig. 6(b).

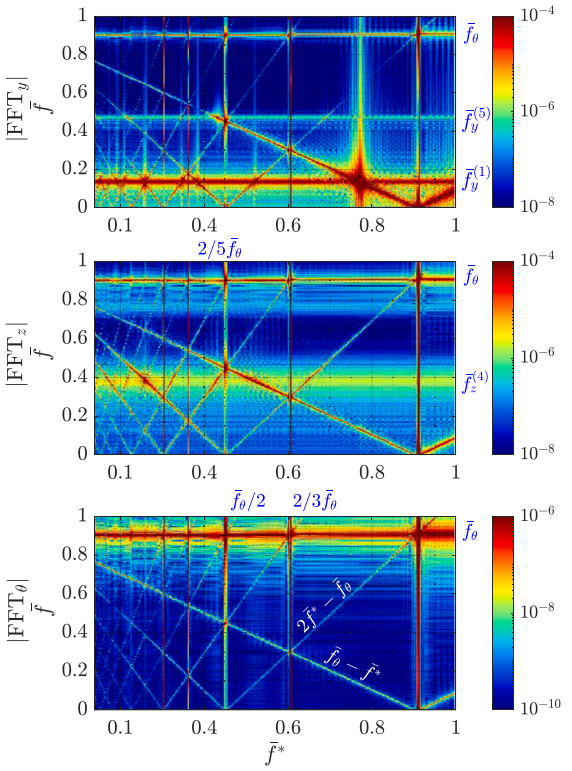

Fig. 8. Fast Fourier transform modulus of bridge mid-span lateral, vertical and torsional buffeting response at $V_m=50$ m/s. The results refer to $\alpha_m=0$ deg and to sinusoidal gust amplitudes and frequencies following the attendant stability boundary [see Fig. 6(b)]. The abscissa is the non-dimensional pumping frequency of the parametric excitation, $\bar{f}^*=f^*/f_{\theta,0}^{(15)}$, while the ordinate is the non-dimensional response frequency, $\bar{f}=f/f_{\theta,0}^{(15)}$.

The previous considerations underscore the potentially pivotal role potentially played by the average parametric effect in governing the stability of the time-variant bridge system described by Eq. (7) and its response, also when subjected to a realistic random noise, such as

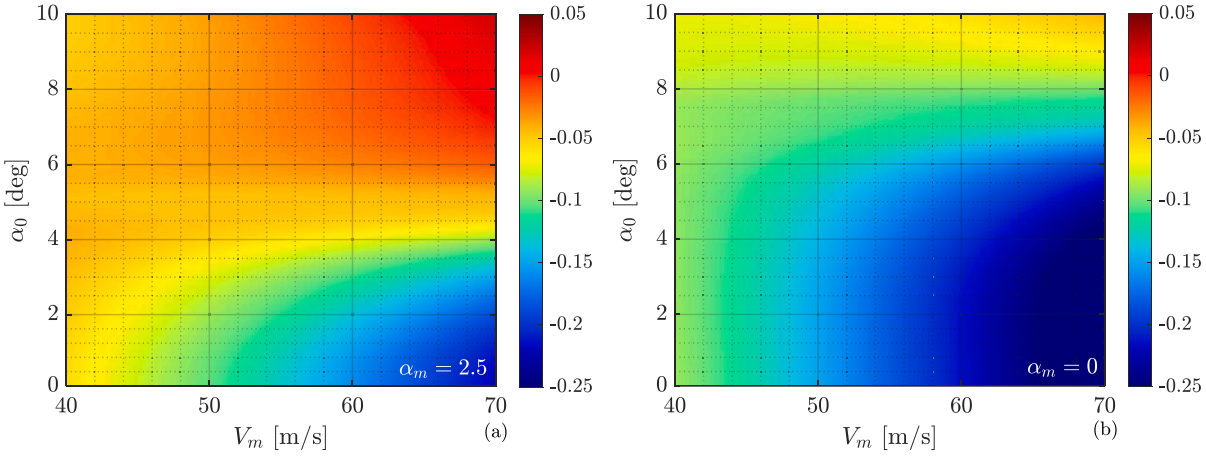

Fig. 7. Map of the average value of A_2^* for a sinusoidal variation of the angle of attack around the mean values $\alpha_m=2.5$ deg (a) and 0 deg (b), as a function of the amplitude α_0 and mean wind velocity V_m. The A_2^* coefficient is evaluated at the reduced velocity $V_r=V_m/(Bf_\theta^{(15)})$.

turbulence. In such a case, the magnitude of the fluctuations in the angle of attack is associated with the turbulence intensity. Furthermore, in a homogeneous random wind field, this effect is invariant along the bridge girder, since it is related to a single-point statistic (the mean) and therefore unaffected by turbulence spatial correlation. This fact easily explains the counterintuitive result of Fig. 3, namely that the bridge buffeting response and flutter stability are essentially independent of the degree of correlation of the parametric variation in the wind angle of attack.

The effects of parametric excitation can also be observed in the buffeting response of the considered time-periodic system (Eq. (7)). Fig. 8 presents the Fourier transform modulus of lateral, vertical, and torsional responses of the bridge mid-span section, for a mean wind velocity of 50 m/s and a null mean angle of attack, $\alpha_m = 0$ deg. Amplitudes, α_0, and pumping frequencies of the parametric excitation, f^*, are chosen so to follow the stability boundary corresponding to the considered mean wind velocity [see Fig. 6(b)]. The resulting time-periodic system is excited by buffeting forces with a white noise spectrum, ensuring a uniform excitation at all frequencies. The parametric excitation induces additional peaks in the response spectrum at $f_\theta + kf^*$ and $f_\theta - kf^*$, where k is a positive integer, visible in the figures in the form of diagonal lines; kf^* represents the k-th order modulation frequency component in the response time histories. In general, the higher the value of k, the lower the energy associated with the attendant modulation component. It can be observed that parametric resonances occur at the intersection of these lines, namely at $f^* = \frac{2}{k+h} f_\theta$, where k and h are positive integers. In addition, the parametric diagonal branches, though related to the torsional motion, also interact with lateral and vertical modes. This interaction results in a more pronounced response, highlighted in the figures with a red colour, particularly when the modulation frequencies approach the frequencies of lateral bending mode, f_y, and vertical bending mode, f_z. This effect may be indicated as *parametric coupling resonance* and might be responsible for the dip in the stability boundaries in Fig. 6(b) around $\bar{f}_\theta{}^* = 0.4$ to 0.5 ($\bar{f} = f/f_{\theta,0}^{(15)}$ denotes the non-dimensional frequency), for mean wind velocities between 50 and 60 m/s. This result shows that parametric excitation could also work as a mechanism of energy transfer between different modes, a concept that complies with the conclusions of Bucher and Lin (1989). Interestingly, this effect can even be observed prior to the onset of instability, indicating its potential influence on the bridge buffeting response when the amplitude of the parametric excitation becomes large.

To sum up, two distinct parametric excitation mechanisms affect the bridge stability. On the one hand, the average parametric effect significantly reduces the overall system damping, leading to an earlier occurrence of "standard" flutter instability. Indeed, as the mean wind velocity approaches the time-invariant critical velocity V_{cr}^{LTI}, the stability boundaries follow an almost horizontal pattern, indicating that flutter arises before the parametric excitation amplitude is such that the parametric resonances are able to play a significant role. Relating the sinusoidal amplitude to the turbulence intensity in a real-world scenario, one may expect that for low turbulence intensity the stability threshold is primarily influenced by the average parametric effect. Conversely, in case of high turbulence intensity, parametric resonances can be effective in reducing the bridge stability, and flutter might occur at wind velocities significantly lower than V_{cr}^{LTI}.

Finally, some effects of the multiple cutoff frequency approach on the stability boundaries are visible in Fig. 6, although relatively minor. The interruption of the parametric excitation related to lateral and vertical motions ($\tilde{\alpha}_y$ and $\tilde{\alpha}_z$) after 0.05 Hz and 0.11 Hz, respectively ($\bar{f}_y^c$ and $\bar{f}_z^c$ in the nondimensional notation of Fig. 6), has an impact on the average parametric effect. Indeed, the aerodynamic derivatives associated with lateral and vertical motion are no longer affected by the average parametric effect when $\tilde{\alpha}_y$ and $\tilde{\alpha}_z$ are identically set to α_m beyond the cutoff frequencies. The evidence of it are the discontinuities in the stability maps for $\bar{f}^* = \bar{f}_y^c$ and $\bar{f}^* = \bar{f}_z^c$. In particular, the boundary upshift after $\bar{f}_y^c$ reveals the destabilising role in this case of the average parametric effect associated with the lateral motion, while the downshift after $\bar{f}_z^c$ underscores the stabilising role of the average parametric effect associated with the vertical motion.

Fig. 9 shows the Floquet stability chart in the case of parametric excitation in the wind velocity magnitude. Mean wind velocities below and above the time-invariant stability limit of 65.1 m/s are considered in Fig. 9(a) and (b), respectively. Compared to the angle-of-attack case, two different sources of parametric excitation are present here, namely the variation in the kinetic pressure and that in the reduced velocity. The former plays the same role as the parameter q in the Hill-type equation presented in Eq. (16), and essentially modulates the magnitude of the self-excited forces, resulting in parametric resonances without any average parametric effect (unless it is associated with other parametric excitations). In contrast, the sinusoidal variation in the reduced velocity may also promote an average parametric effect; nevertheless, this is expected to be modest due to the nearly linear local trend of the aerodynamic derivatives with the reduced velocity. The parametric resonances associated with lateral and vertical modes are more evident in Fig. 9(a) than in Fig. 6. This may be attributed to the contribution of the

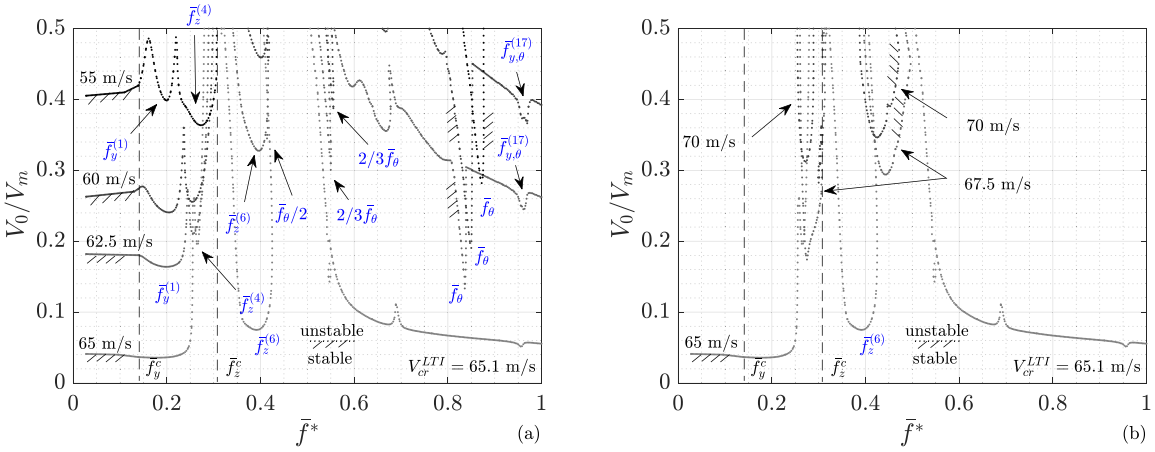

Fig. 9. Stability chart of the Hardanger Bridge for different amplitudes and frequencies of the perfectly correlated sinusoidal variation in the wind velocity magnitude appearing in the self-excited forces for various mean wind speeds. V_{cr}^{LTI} represents the time-invariant flutter threshold. The results refer to $\alpha_m = 2.5$ deg. The nondimensional pumping frequency is defined as $\bar{f}^* = f^*/f_{\theta,0}^{(15)}$; the mode vibration frequencies are normalised in the same way.

kinetic pressure fluctuation. In addition, as already observed in Fig. 6, a progressive decrease in the torsional frequency with the mean wind velocity is apparent due to the influence of the aerodynamic stiffness. A similar effect can also be observed for the V-shaped lateral and vertical parametric resonances. However, this feature can be attributed to an increase in modal aerodynamic damping with V_m, which can result in a left or right shift of the parametric resonances compared to the undamped condition (see, e.g., the Mathieu stability chart in Nayfeh and Mook, 2008). Interestingly, the two stable regions located slightly below and slightly above the frequency of vertical mode 6, and associated with mean wind velocities higher than the time-invariant stability threshold (Fig. 9(b)), demonstrate the presence of stabilising parametric effects too. Finally, large amplitudes of oscillation of the wind velocity magnitude are required to produce significant parametric effects on the flutter stability and, except for mean wind velocities very close to the linear time-invariant threshold, such amplitudes cannot be associated with realistic turbulence intensities. Therefore, the parametric excitation due to wind velocity magnitude fluctuations plays a secondary role compared to that arising from the variation in the angle of attack. This result complies with what was observed in the buffeting response in Fig. 3, where most of the parametric effect of large-scale turbulence was clearly ascribed to the slowly-varying angle of attack.

6. Equivalent time-invariant model

Based on previous considerations on the prominent role of the average parametric effect (especially for realistic not too large turbulence intensity and integral length scale) associated with the a slow variation in the angle of attack and on its independence of wind field spanwise correlation, it seems reasonable to disregard parametric resonances (either coupled or not) and account for the average parametric effect of large-scale turbulence by slightly modifying Scanlan's classical linear time-invariant model. Indeed, the bridge buffeting response and the flutter stability can simply be determined using the aerodynamic derivatives averaged over the time histories of the slowly-varying angle of attack, defining what we may call the "equivalent linear time-invariant model" (LTI_{eq}). Clearly, such an average depends on the probability distribution function (PDF) of $\widetilde{\alpha}(t)$ and not only on its amplitude like in the time-periodic case of Section 5.2. In addition, average aerodynamic derivatives should be derived from $\widetilde{\alpha}_y, \widetilde{\alpha}_z$ and $\widetilde{\alpha}_\theta$, based on the motion components they are associated with. The low-pass filters with fixed cutoff frequencies also result in slightly different average aerodynamic coefficients depending on the mean wind velocity, requiring specific calculations in each case. In order to do so, the time history of each aerodynamic derivative can be evaluated according to the 2D RFA model and then averaged over time to obtain the average aerodynamic damping $\overline{\mathbf{C}}_{ae}$ and stiffness $\overline{\mathbf{K}}_{ae}$, as shown by the following equations:

$$\overline{\mathbf{C}_{ae}(\widetilde{\alpha})} = \overline{\left[\frac{1}{K}\left(\mathbf{A}_2(\widetilde{\alpha}) + \sum_{l=1}^{N-2}\mathbf{A}_{l+2}(\widetilde{\alpha})\frac{d_l(\widetilde{\alpha})}{d_l(\widetilde{\alpha})^2 + K^2}\right)\right]} \tag{17}$$

$$\overline{\mathbf{K}_{ae}(\widetilde{\alpha})} = \overline{\left[\frac{1}{K^2}\left(\mathbf{A}_1(\widetilde{\alpha}) + \sum_{l=1}^{N-2}\mathbf{A}_{l+2}(\widetilde{\alpha})\frac{K^2}{d_l(\widetilde{\alpha})^2 + K^2}\right)\right]} \tag{18}$$

where the overbar denotes again the time-average operator. However, once the time histories of slowly varying angles of attack $\widetilde{\alpha}_y, \widetilde{\alpha}_z$ and $\widetilde{\alpha}_\theta$ are obtained for a generic point of the bridge, $\overline{\mathbf{C}_{ae}(\widetilde{\alpha})}$ and $\overline{\mathbf{K}_{ae}(\widetilde{\alpha})}$ can easily be determined by a numerical interpolation of experimental aerodynamic derivatives for different angles of attack without implementing the 2D RFA model as done in the current work for the sake of comparison with the linear time-variant results. A few examples for three different turbulent wind fields and a mean wind velocity of 50 m/s are reported in Fig. 10. For large turbulence intensity and integral length scale, the average coefficient A_2^* progressively increases and can even become positive, assuming values significantly different from those evaluated at the mean angle of attack, α_m= 2.5 deg. The LTI_{eq} approach leads to a time-invariant state matrix, which allows for a straightforward deterministic flutter stability assessment. In particular, the average aerodynamic derivatives can also be utilised in simple frequency-domain calculations.

Fig. 11 compares the bridge torsional response obtained with the LTI_{eq} model and those obtained with the classical LTI model and with the full LTV model for various turbulence intensities and integral length scales. Clearly, the LTI_{eq} approach is not only able to predict the LTV flutter stability threshold but also to provide a good approximation of the buffeting response. In the worst-case scenario, the LTI_{eq} model can

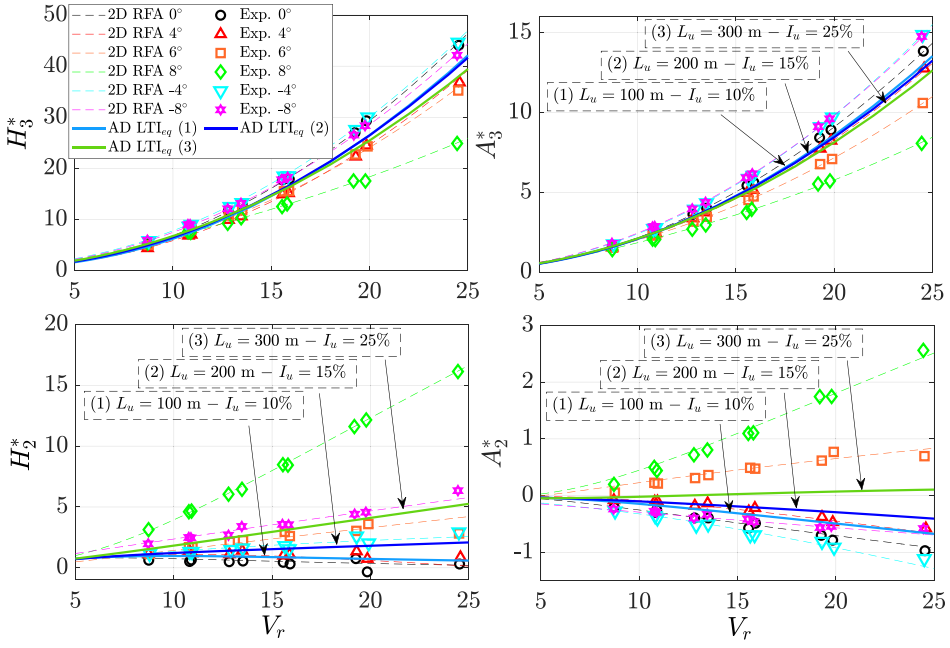

Fig. 10. Lift and moment aerodynamic derivatives of the Hardanger Bridge associated with the torsional motion. Comparison between the measured coefficients for various mean angles of attack and those averaged over the time history of the slowly-varying angle of attack $\widetilde{\alpha}_\theta$ for a mean wind velocity of 50 m/s.

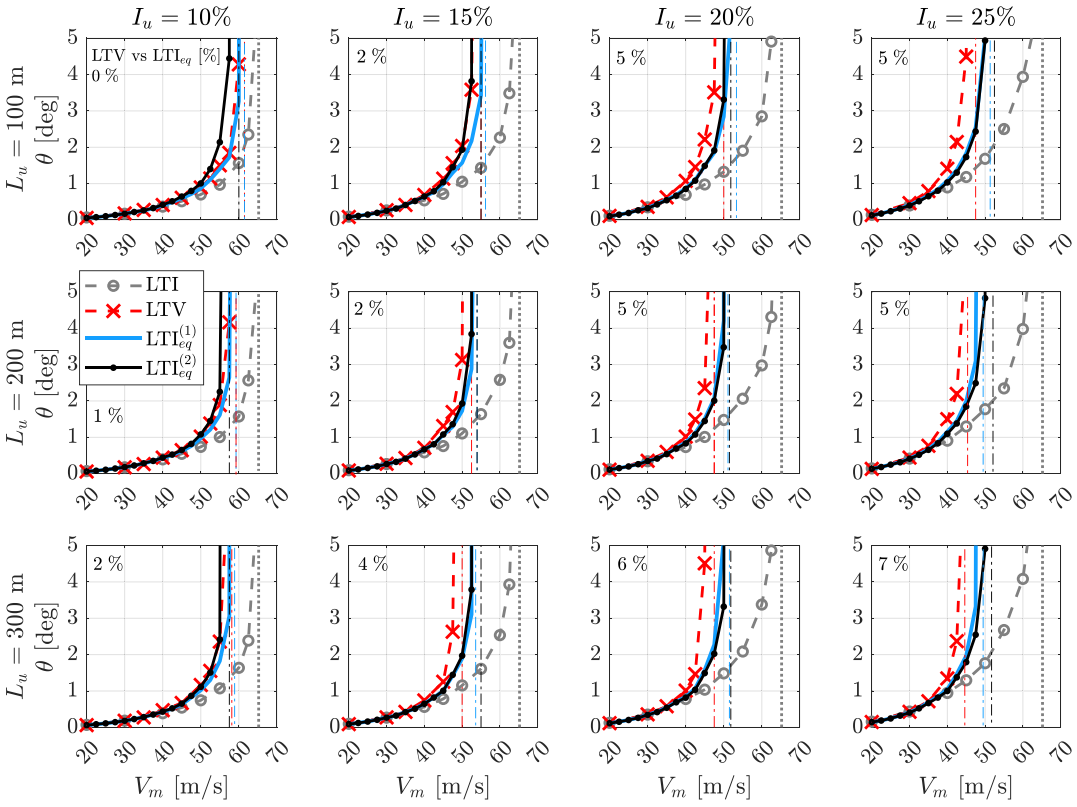

Fig. 11. RMS of mid-span nonlinear buffeting torsional response at mid-span of the Hardanger Bridge. The grey circles refer to the results obtained with the classical linear time-invariant (LTI) approach; the red crosses to the results of the linear time-variant (LTV) model, considering only the self-excited force modulation due to the angle of attack; the thick light blue line and the thin black line with small dots correspond to the torsional response obtained by averaging the aerodynamic derivatives according to the LTI$_{eq}$ (considering only the low-frequency components of the wind angle of attack in the first case, LTI$_{eq}^{(1)}$, and the whole spectrum in the second case, LTI$_{eq}^{(2)}$). The percentages in the top-left corner of each frame indicates the overestimation of the LTV flutter threshold by the LTI$_{eq}$ approach.

account for approximately three quarters of the reduction in critical mean wind velocity caused by the parametric effect of turbulence. This conclusion complies with the stability maps in Fig. 6(a). Indeed, as explained above, the stability threshold for a mean wind velocity between 50 and 65 m/s, associated with moderate turbulence intensity, is primarily determined by the average parametric effect. Consequently, a close correspondence between LTI$_{eq}$ and LTV flutter thresholds is expected when it occurs in this mean wind velocity range. In contrast, for high turbulence intensity and large integral length scale, when the flutter threshold is remarkably reduced compared to the smooth flow condition and the critical wind velocity is below 50 m/s, the parametric resonance effects become nonnegligible. This leads to a slightly less good agreement between LTI$_{eq}$ and LTV results. Nevertheless, in the present case the LTI$_{eq}$ approach never overestimates the flutter critical wind speed by more than 7%. By comparing Figs. 3 and 11, it is possible to note that the effect of partial spanwise correlation of the parametric excitation is negligible even when there is a nonnegligible difference between LTI$_{eq}$ and LTV results. Then, one may conjecture that also the effect of parametric resonances is practically independent of random wind field correlation.

Given also the abovementioned partial arbitrariness of the range of turbulent scales that are effective in parametrically exciting the bridge, for the sake of simplicity, one may also consider the entire turbulence spectrum without applying any cutoff frequencies. In addition, assuming that the probability distribution of the angle of attack coincides with that of vertical turbulence (i.e., $\alpha = \text{atan}\left(\frac{w}{V_m+u}\right) \cong \frac{w}{V_m}$) and is therefore Gaussian, the average aerodynamic derivatives can be calculated in a straightforward way (with no need for simulated wind angle of attack time histories), as follows:

$$\overline{\mathbf{C}}_{ae} = \mathrm{E}[\mathbf{C}_{ae}(\alpha)] = \int \mathbf{C}_{ae}(\alpha) p(\alpha) d\alpha \tag{19}$$

$$\overline{\mathbf{K}}_{ae} = \mathrm{E}[\mathbf{K}_{ae}(\alpha)] = \int \mathbf{K}_{ae}(\alpha) p(\alpha) d\alpha \tag{20}$$

$$p(\alpha) = \frac{1}{I_w\sqrt{2\pi}} \exp\left[-\frac{1}{2}\left(\frac{\alpha-\alpha_m}{I_w}\right)^2\right] \tag{21}$$

where E[·] stands for the ensemble average operator, and $p(\alpha)$ for the probability density function of the wind angle of attack. The results obtained with these average aerodynamic derivatives are also reported in Fig. 11; they are very close to those provided by the reference LTI$_{eq}$ approach (based on the multiple cutoff strategy) for most integral length scales and turbulence intensities. However, nonnegligible differences are apparent when the integral length scale and the turbulence intensity are small. In the first case, clearly the variance of the parametric variation in the angle of attack is significantly larger when the cutoffs are disregarded. In contrast, when the turbulence intensity is low the bridge is stable up to a mean wind velocity very close to V_{cr}^{LTI}; in this condition, a small change in the average aerodynamic derivatives and therefore in the average parametric effect is able to produce a nonnegligible shift in the stability boundary.

Finally, it is important to highlight that the proposed simplified approach does not consider the bridge stochastic stability in terms of higher-order statistical moments, even though they may become relevant in certain conditions (e.g., temporary states of instability). Higher-

order statistics can also be significant in characterising the probability distribution of the maximum bridge response (see Barni et al., 2022), which is crucial for bridge design. However, this issue seems to affect the bridge response only close to the flutter stability threshold, thus making the limitations of the LTI_{eq} approach acceptable for most practical applications.

7. Conclusions

The parametric effects induced by large-scale turbulence on the flutter stability of suspension bridges has been investigated, considering the Hardanger Bridge as a case study. This problem has been addressed with a linear time-variant state-space model and solved with a Monte Carlo approach for different turbulent wind fields. The Floquet theory has been employed to investigate the same dynamic system but with a simplified time-periodic parametric excitation to shed some light on the observed destabilising effects induced by turbulence. Floquet multipliers have proven to be a valuable tool for underscoring the hidden parametric excitation mechanisms affecting bridge flutter stability.

The main conclusions of the work are summarised here below. They directly refer to the Hardanger Bridge case study, but many of them can also be extended to other bridges, with the awareness that specific effects may vary based mainly on the characteristics of the aerodynamic derivatives.

- The parametric excitation of large-scale turbulence, which produces slow fluctuations in both wind velocity magnitude and angle of attack, can have a significant impact on the bridge flutter stability, especially for high turbulence intensity and large integral length scale. However, the role of the angle of attack seems to be dominant. In particular, a marked destabilising effect was observed for the Hardanger Bridge case study.
- The parametric excitation due to wind turbulence can affect the flutter stability based on two mechanisms, namely the parametric resonances (either coupled or not) and the average parametric effect. These phenomena play a destabilising role for this case study. In particular, inspection of stability charts for a time-periodic system highlighted the prominent role of the average parametric effect, driving the instability when the mean wind velocity gets close to the linear time-invariant threshold.
- When the aerodynamic derivatives present a strongly nonlinear and non-antisymmetric pattern with the mean angle of attack, as in the case of the Hardanger Bridge, the average parametric effect associated with the angle of attack may significantly affect the buffeting response and the flutter stability of the bridge. In contrast, for fairly streamlined bridge sections important aerodynamic derivatives tend to exhibit a pattern with the reduced wind velocity that is not too far from linear; consequently, the average parametric effect associated with the wind velocity magnitude is likely to be modest.
- Since the average parametric effect is associated with a single-point statistic, the spatial correlation of the parametric excitation does not play a significant role in the flutter stability mechanism and buffeting response, thereby explaining the counterintuitive result obtained with Monte Carlo simulations. This fact also emphasises the potentially strong impact (either beneficial or detrimental) of the parametric effect of turbulence on the actual stability of long-span suspension bridges.
- The equivalent linear time-invariant (LTI_{eq}) approach is an effective simple alternative to the linear time-variant (LTV) approach for analysing both the buffeting response and the flutter stability of suspension bridges under typical turbulent flow conditions. It is also worth noting that the average aerodynamic derivatives to be used in the LTI_{eq} approach do not depend on the specific model adopted for self-excited forces but just on the pattern of the aerodynamic derivatives with the mean angle of attack, as long as the model relies on the assumption of slow variations in the angle of attack due to atmospheric turbulence.
- For high turbulence intensity and large integral length scale (i.e., for high magnitude of the parametric excitation), the accuracy of the LTI_{eq} approach in predicting the flutter stability threshold and the buffeting response slightly deteriorates due to the effect of coupling and torsional parametric resonances. However, the differences remain relatively small for the Hardanger Bridge, even considering a longitudinal turbulence intensity of 25% and an integral length scale of 300 m. Some discrepancies in terms of probability distribution of bridge response maxima are also observed close to flutter.
- The choice of the cutoff frequencies in the 2D RFA model (or in similar models) remains an open issue that needs to be addressed, especially considering that the spatial correlation of wind velocity fluctuations does not influence the average parametric effect and then, in this respect, it does not represent a filtering mechanism for turbulent scales. It is then natural to wonder which are the turbulent scales that can truly modulate the self-excited forces. This issue calls for specific experimental studies in the future.
- Simple calculations carried out with the LTI_{eq} approach considering the parametric excitation associated with the entire turbulent wind spectrum offered results in close agreement with those obtained based on the multiple cutoff strategy, especially for not-so-low turbulence intensity and integral length scale. This fact highlights the robustness of the analysis performed in this work and of the conclusions deduced from it.
- The possibility of having a more stable or unstable average set of aerodynamic derivatives compared to those evaluated at the steady-state deck rotation and wind incidence explains, to a large extent, how atmospheric turbulence can either stabilise or destabilise a bridge. This change of perspective also impacts on self-excited force measurement in turbulent flow. Indeed, leaving aside here the important pure aerodynamic effect stemming from the interaction of small-scale turbulence with separated shear layers, aerodynamic derivatives identified in turbulent flow can be interpreted as the modified coefficients accounting for the abovementioned average parametric effect as long as the turbulence characteristics in the wind tunnel, namely turbulence intensity and integral length scale, are correctly physically modelled.
- The dependence of the average parametric effect on the integral length scale of turbulence is only dictated by the cutoffs used to isolate the large scales. Indeed, in the spirit of all band-superposition models, these are the only turbulent scales considered effective for the parametric excitation of a bridge structure.
- Although the 2D RFA model has carefully been validated through experiments (Barni et al., 2021; Barni, 2022), a final wind tunnel test able to demonstrate the validity of the conclusions reported in the current work is still missing. Several possible pitfalls can be envisaged for such an experiment, which represents a decisive development of this line of research.
- Finally, the findings of this study contradict the long-standing belief that aerodynamic derivatives measured in a smooth flow (and subsequently used in the framework of classical linear time-invariant models) are generally conservative.

CRediT authorship contribution statement

Niccolò Barni: Conceptualization, Methodology, Software, Formal analysis, Validation, Visualization, Writing – original draft. **Claudio Mannini:** Conceptualization, Methodology, Supervision, Validation, Writing – review & editing, Funding acquisition.

Declaration of competing interest

The authors declare that they have no known competing financial interests or personal relationships that could have appeared to influence

the work reported in this paper.

Data availability

Data will be made available on request.

APPENDIX A. FLOQUET THEORY

Due to the periodicity assumption for the parametric excitation [Eq. (12)], the state matrix is also periodic: $\mathbf{\Omega}(t) = \mathbf{\Omega}(t+T^*)$; then, Floquet's theorem (Richards, 1983) states that the state-transition matrix can be diagonalised as follows:

$$\mathbf{\Phi}_{\mathbf{\Omega}}(t,t_0) = \mathbf{\Psi}(t)\exp[\mathbf{\Gamma}(t)\cdot(t-t_0)]\mathbf{\Psi}(t_0)^{-1} \tag{A1}$$

where $\mathbf{\Psi}(t)$ is the periodic modal matrix (Floquet modes) of the state-transition matrix, and $\mathbf{\Gamma}(T^*)$ is a diagonal matrix containing the Floquet exponents $\upsilon_1,\upsilon_2,\ldots,\upsilon_n$. The eigenvalues of the monodromy matrix $\mathbf{\Phi}_{\mathbf{\Omega}}(T^*,0)$, namely the complex numbers $\varsigma_1,\varsigma_2,\ldots,\varsigma_n$, are called Floquet multipliers, and are related to the Floquet exponents by $\upsilon_j = \frac{\ln(\varsigma_j)}{T^*}$. The location of the Floquet multipliers with respect to the unit circle in the complex plane rules the stability of a linear time-periodic system. Indeed, a Floquet multiplier outside the unit circle ($|\varsigma_j| > 1$) leads to an asymptotically unstable response in the direction of the corresponding Floquet eigenvector $\boldsymbol{\psi}_j(T^*)$. Therefore, once the monodromy state-transition matrix is known, system stability can be determined by looking at the Floquet multipliers. $\mathbf{\Phi}_{\mathbf{\Omega}}(T^*,0)$ can be obtained by numerical integration of Eq. (7) over a period T^*. However, based on Eq. (14), integrating in discrete time, the state-transition matrix can efficiently be calculated by:

$$\mathbf{\Phi}_{\mathbf{\Omega}}(s,0) = \begin{cases} \mathbf{\Omega}(s-1)\mathbf{\Omega}(s-2)\ldots\mathbf{\Omega}(0) & s \geq 1 \\ \mathbf{I} & s = 0 \end{cases} \tag{A2}$$

The stability of the time-periodic system can be studied for various pumping frequencies ($f^* = 1/T^*$) and intensities (amplitudes) of the parametric excitation through charts where, for each mean wind speed, the conditions $\max_j\left[|\varsigma_j(V_0,f^*)|\right] > 1$ or $\max_j\left[|\varsigma_j(\alpha_0,f^*)|\right] > 1$ identify the unstable regions.

References

Aas-Jakobsen, K., Strømmen, E., 2001. Time domain buffeting response calculations of slender structures. J. Wind Eng. Ind. Aerod. 89 (5), 341–364.

Argentini, T., Pagani, A., Rocchi, D., Zasso, A., 2014. Monte Carlo analysis of total damping and flutter speed of a long span bridge: effects of structural and aerodynamic uncertainties. J. Wind Eng. Ind. Aerod. 128, 90–104.

Argentini, T., Rocchi, D., Somaschini, C., 2020. Effect of the low-frequency turbulence on the aeroelastic response of a long-span bridge in wind tunnel. J. Wind Eng. Ind. Aerod. 197, 104072.

Arnold, L., 1984. Formula connecting sample and moment stability of linear stochastic. SIAM J. Appl. Math. 44 (4), 793–802.

Arnold, L., Papanicolaou, G., Wihstutz, V., 1986. Asymptotic analysis of the Lyapunov exponent and rotation number of the random oscillator and applications. SIAM J. Appl. Math. 46 (3), 427–450.

Barni, N., Øiseth, O., Mannini, C., 2021. Time-variant self-excited force model based on 2D rational function approximation. J. Wind Eng. Ind. Aerod. 211, 104523.

Barni, N., Øiseth, O.A., Mannini, C., 2022. Buffeting response of a suspension bridge based on the 2D rational function approximation model for self-excited forces. Eng. Struct. 261, 114267.

Barni, N., 2022. Long Span Bridge Buffeting Response in Turbulent Flow. Ph. D. thesis, University of Florence, Italy – Norwegian University of Science and Technology, Norway.

Barni, N., Øiseth, O., Mannini, C., 2023a. Nonlinear buffeting response of long suspension bridges considering parametric excitation due to large-scale turbulence. In: *IABSE Symposium Istanbul 2023: Long Span Bridges - Proceeding Book*, Istanbul, Turkey, April 26-28, 2023, pp. 351–358.

Barni, N., Øiseth, O., Petersen, Ø., Mannini, C., 2023b. Nonlinear buffeting modelling of a 2000 m long twin-deck suspension bridge. In: Proceedings of the 16th International Conference on Wind Engineering. ICWE, August 27-31, 2023, Florence, Italy.

Bartoli, G., Borri, C., Gusella, V., 1997. On the influence of wind turbulence on bridge deck flutter. In: Meskouris, K., Vittek, U. (Eds.), Aspects in Modern Computational Structural Analysis. Balkema, Rotterdam, The Netherlands, pp. 3–17.

Bartoli, G., Mannini, C., 2008. A simplified approach to bridge deck flutter. J. Wind Eng. Ind. Aerod. 96 (2), 229–256.

Bearman, P.W., Morel, T., 1983. Effect of free stream turbulence on the flow around bluff bodies. Prog. Aero. Sci. 20 (2–3), 97–123.

Bocciolone, M., Cheli, F., Curami, A., Zasso, A., 1992. Wind measurements on the Humber bridge and numerical simulations. J. Wind Eng. Ind. Aerod. 42 (1–3), 1393–1404.

Bogoliubov, N.N., Mitroplosky, Y.A., 1961. Asymptotic Method in the Theory of Nonlinear Oscillations. Gordon & Breach Science Publishers Ltd, New York, US.

Bucher, C.G., Lin, Y.K., 1988a. Stochastic stability of bridges considering coupled modes. J. Eng. Mech. 114 (12), 2055–2071.

Bucher, C.G., Lin, Y.K., 1988b. Effect of spanwise correlation of turbulence field on the motion stability of long-span bridges. J. Fluid Struct. 2 (5), 437–451.

Bucher, C.G., Lin, Y.K., 1989. Stochastic stability of bridges considering coupled modes: II. J. Eng. Mech. 115 (2), 384–400.

Canor, T., Caracoglia, L., Denoël, V., 2015. Application of random eigenvalue analysis to assess bridge flutter probability. J. Wind Eng. Ind. Aerod. 140, 79–86.

Caracoglia, L., 2013. An Euler-Monte Carlo algorithm assessing moment lyapunov exponents for stochastic bridge flutter predictions. Comput. Struct. 122, 65–77.

Caracoglia, L., Sarkar, P.P., Haan Jr., F.L., Sato, H., Murakoshi, J., 2009. Comparative and sensitivity study of flutter derivatives of selected bridge deck sections, part 2: implications on the aerodynamic stability of long-span bridges. Eng. Struct. 31 (9), 2194–2202.

Chen, X., Kareem, A., 2001. Nonlinear response analysis of long-span bridges under turbulent winds. J. Wind Eng. Ind. Aerod. 89 (14–15), 1335–1350.

Chen, X., Kareem, A., 2003. Aeroelastic analysis of bridges: effects of turbulence and aerodynamic nonlinearities. J. Eng. Mech. 129 (8), 885–895.

Chen, X., Kareem, A., 2006. Revisiting multimode coupled bridge flutter: some new insights. J. Eng. Mech. 132 (10), 1115–1123.

Chen, X., 2014. Analysis of multimode coupled buffeting response of long-span bridges to nonstationary winds with force parameters from stationary wind. J. Struct. Eng. 141 (4), 04014131.

Davenport, A.G., 1962. Buffetting of a suspension bridge by storm winds. J. Struct. Div. 88 (3), 233–270.

Diana, G., Bruni, S., Cigada, A., Collina, A., 1993. Turbulence effect on flutter velocity in long span suspended bridges. J. Wind Eng. Ind. Aerod. 48 (2–3), 329–342.

Diana, G., Falco, M., Bruni, S., Cigada, A., Larose, G.L., Damsgaard, A., Collina, A., 1995. Comparisons between wind tunnel tests on a full aeroelastic model of the proposed bridge over Stretto di Messina and numerical results. J. Wind Eng. Ind. Aerod. 54, 101–113.

Diana, G., Rocchi, D., Argentini, T., 2013. An experimental validation of a band superposition model of the aerodynamic forces acting on multi-box deck sections. J. Wind Eng. Ind. Aerod. 113, 40–58.

Diana, G., Stoyanoff, S., Aas-Jakobsen, K., Allsop, A., Andersen, M., Argentini, T., et al., 2019. IABSE Task Group 3.1 benchmark results. Part 1: numerical analysis of a two-degree-of-freedom bridge deck section based on analytical aerodynamics. Struct. Eng. Int. 30 (3), 401–410.

Diana, G., Stoyanoff, S., Aas-Jakobsen, K., Allsop, A., Andersen, M., Argentini, T., et al., 2020. IABSE Task Group 3.1 benchmark results. Part 2: numerical analysis of a three-degree-of-freedom bridge deck section based on experimental aerodynamics. Struct. Eng. Int. 30 (3), 411–420.

Diana, G., Omarini, S., 2020. A nonlinear method to compute the buffeting response of a bridge validation of the model through wind tunnel tests. J. Wind Eng. Ind. Aerod. 201, 104163.

Fenerci, A., Øiseth, O., 2017. Measured buffeting response of a long-span suspension bridge compared with numerical predictions based on design wind spectra. J. Struct. Eng. 143 (9), 04017131.

Fenerci, A., Øiseth, O., 2018. Strong wind characteristics and dynamic response of a long-span suspension bridge during a storm. J. Wind Eng. Ind. Aerod. 172, 116–138.

Gao, G., Zhu, L., Li, J., Han, W., 2020. Application of a new empirical model of nonlinear self-excited force to torsional vortex-induced vibration and nonlinear flutter of bluff bridge sections. J. Wind Eng. Ind. Aerod. 205, 104313.
Grigoriu, M., 2002. Stochastic Calculus. Applications in Science and Engineering. Birkhäuser, Boston, US.
Hu, L., Xu, Y.L., Huang, W.F., 2013. Typhoon-induced nonstationary buffeting response of long-span bridges in complex terrain. Eng. Struct. 57, 406–415.
Irwin, H.P.A.H., Schuyler, G.D., 1978. Wind effects on a full aeroelastic bridge model. In: ASCE *Spring Convention And Exhibit*, Preprint 3268, Pittsburgh, US, April 24-28, 1978.
Jain, A., Jones, N.P., Scanlan, R.H., 1996. Coupled flutter and buffeting analysis of long-span bridges. J. Struct. Eng. 122 (7), 716–725.
Katsuchi, H., Jones, N.P., Scanlan, R.H., 1999. Multimode coupled flutter and buffeting analysis of the Akashi-Kaikyo Bridge. J. Struct. Eng. 125 (1), 60–69.
Kozin, F., 1967. A survey of stability of stochastic systems. Automatica 5, 95–112.
Lander, D., Letchford, C., 2023. Towards understanding the effects of freestream turbulence on separation bubble dynamics beyond integral parameters. In: Proceedings of the 16th International Conference on Wind Engineering. ICWE16, August 27-31, 2023, Florence, Italy.
Li, Q.C., Lin, Y.K., 1995. New stochastic theory for bridge stability in turbulent flow. II. J. Eng. Mech. 121 (1), 102–116.
Lin, Y.K., 1996. Stochastic stability of wind-excited long-span bridges. Probabilist. Eng. Mech. 11 (4), 257–261.
Lin, Y.K., Ariaratnam, S.T., 1980. Stability of bridge motion in turbulent winds. J. Struct. Mech. 8 (1), 1–15.
Lin, Y.K., Li, Q.C., 1993. New stochastic theory for bridge stability in turbulent flow. J. Eng. Mech. 119 (1), 113–127.
Lystad, T.M., Fenerci, A., Øiseth, O., 2020. Buffeting response of long-span bridges considering uncertain turbulence parameters using the environmental contour method. Eng. Struct. 213, 110575.
Mannini, C., Bartoli, G., 2015. Aerodynamic uncertainty propagation in bridge flutter analysis. Struct. Saf. 52 (Part A), 29–39.
Mannini, C., Sbragi, G., Schewe, G., 2016. Analysis of self-excited forces for a box-girder bridge deck through unsteady RANS simulations. J. Fluid Struct. 63, 57–76.
Mannini, C., Massai, T., Marra, A.M., 2018. Unsteady galloping of a rectangular cylinder in turbulent flow. J. Wind Eng. Ind. Aerod. 173, 210–226.
Nayfeh, A.H., Mook, D.T., 2008. Nonlinear Oscillations. John Wiley & Sons.
Poirel, D.C., Price, S.J., 2001. Structurally nonlinear fluttering airfoil in turbulent flow. AIAA J. 39 (10), 1960–1968.
Poirel, D., Price, S.J., 2003. Random binary (coalescence) flutter of a two-dimensional linear airfoil. J. Fluid Struct. 18 (1), 23–42.
Rizzo, F., Caracoglia, L., 2018. Examination of experimental errors in scanlan derivatives of a closed-box bridge deck. Wind Struct. 26 (4), 231–251.
Richards, J.A., 1983. Analysis of Periodically Time-Varying Systems. Springer Science & Business Media.
Roger, K.L., 1977. Airplane Math Modeling and Active Aeroelastic Control Design, vol. 228. AGARD-CP-, pp. 1–11.
Sarkar, P.P., Caracoglia, L., Haan Jr., F.L., Sato, H., Murakoshi, J., 2009. Comparative and sensitivity study of flutter derivatives of selected bridge deck sections, Part 1: analysis of inter-laboratory experimental data. Eng. Struct. 31 (1), 158–169.
Scanlan, R.H., 1997. Amplitude and turbulence effects on bridge flutter derivatives. J. Struct. Eng. 123 (2), 232–236.
Scanlan, R.H., 1978. The action of flexible bridges under wind, I: flutter theory. J. Sound Vib. 60 (2), 187–199.
Scanlan, R.H., Lin, W., 1978. Effects of turbulence on bridge flutter derivatives. J. Eng. Mech. 104 (4), 719–733.
Seo, D.W., Caracoglia, L., 2011. Estimation of torsional-flutter probability in flexible bridges considering randomness in flutter derivatives. Eng. Struct. 33 (8), 2284–2296.
Shinozuka, M., Jan, C.M., 1972. Digital simulation of random processes and its applications. J. Sound Vib. 25 (1), 111–128.
Skyvulstad, H., Argentini, T., Zasso, A., Øiseth, O., 2021. Nonlinear modelling of aerodynamic self-excited forces: an experimental study. J. Wind Eng. Ind. Aerod. 209, 104491.
Skyvulstad, H., Petersen, Ø.W., Argentini, T., Zasso, A., Øiseth, O., 2023. Regularised Volterra series models for modelling of nonlinear self-excited forces on bridge decks. Nonlinear Dynam. 111, 12699–12731.
Tsiatas, G., Sarkar, P.P., 1988. Motion stability of long-span bridges under gusty winds. J. Eng. Mech. 114 (2), 257–276.
Xie, W.C., 2006. Dynamic Stability of Structures. Cambridge University Press.
Ying, Z.G., Ni, Y.Q., Fan, L., 2019. Parametrically excited stability of periodically supported beams under longitudinal harmonic excitations. Int. J. Struct. Stabil. Dynam. 19 (9), 1950095.